

# Differential Dynamic Causal Nets: Model Construction, Identification and Group Comparisons

Kang You<sup>1</sup>, Gary Green<sup>2,3</sup>, Jian Zhang<sup>1,\*</sup>

**1** School of Engineering, Mathematics and Physics, University of Kent, Canterbury, Kent CT2 7NF, UK.

**2** York Neuroimaging Centre, The Biocentre, York Science Park, University of York, Heslington, York YO10 5NY, UK.

**3** Innovision IP Ltd, Culham Innovation Centre, D5 Culham Science Centre, Abingdon, Oxfordshire, OX14 3DB, UK.

\* Corresponding author: Jian Zhang (J.Zhang-79@kent.ac.uk)

## Abstract

Pathophysiological modelling of brain systems from microscale to macroscale remains difficult in group comparisons partly because of the infeasibility of modelling the interactions of thousands of neurons at the scales involved. Here, to address the challenge, we present a novel approach to construct differential causal networks directly from electroencephalogram (EEG) data. The proposed network is based on conditionally coupled neuronal circuits which describe the average behaviour of interacting neuron populations that contribute to observed EEG data. In the network, each node represents a parameterised local neural system while directed edges stand for node-wise connections with transmission parameters. The network is hierarchically structured in the sense that node and edge parameters are varying in subjects but follow a mixed-effects model. A novel evolutionary optimisation algorithm for parameter inference in the proposed method is developed using a loss function derived from Chen-Fliess expansions of stochastic differential equations. The method is demonstrated by application to the fitting of coupled Jansen-Rit local models. The performance of the proposed method is evaluated on both synthetic and real EEG data. In the real EEG data analysis, we track changes in the parameters that characterise dynamic causality within brains that demonstrate epileptic activity. We show evidence of network functional disruptions, due to imbalance of excitatory-inhibitory interneurons and altered epileptic brain connectivity, before and during seizure periods.

**Key words:** Differential network of dynamic causal models, M/EEG scans, epileptic brain network, dynamic causal nets, and mixed-effects models.

## 1 Introduction

Non-invasive imaging techniques electro- and magneto-encephalography (EEG and MEG) are often used for dynamic causal discovery and causality quantification in group comparison with neurological disorders such as stroke, motor neuron disease, Alzheimer's disease, Parkinson's disease, and epilepsy (Choi et al., 2023; Aljalal et al., 2022; Ghassemkhani et al., 2025; Pyrzowski et al., 2015; Ogrim et al., 2012; Rosch et al., 2018) among others. M/EEG are promising tools for studying brain dynamics and

enable researchers and clinicians to measure and characterise brain activity in fine temporal detail thus improving the understanding of the etiology of neurological conditions as well as allowing the development of brain-based technologies.

M/EEG imaging revealed a rich catalogue of behaviour in both resting and active brains. For example, Papadopoulou et al. (2015) used spectral EEG data to profile epileptic seizure activity in the brain. Özbeş et al. (2015) demonstrated that the frontal alpha/theta power ratio derived from the resting-state EEG data is a promising biomarker for distinguishing early-onset Alzheimer's disease from healthy controls. Duffy and Als (2012) found that EEG spectral coherence discriminates children with autism from healthy controls.

Using MEG spectral data, van Es et al. (2025) showed that, although brain network dynamics are stochastic, their activities have a robust cyclical pattern. Zhang and Green (2025) proposed a novel method for detecting mild traumatic brain injury by using spectral likelihood ratio statistics of MEG scan data when controls are not homogenous.

Complementary to the aforementioned spectral analysis, dynamic causal modelling (DCM) of E/MEG data offers a powerful way to infer effective connectivity within the brain through coupled neuronal circuits with certain biophysics-informed parameters that are responsible for what are observed in the brain (Friston et al., 2003; Kiebel et al., 2008; Grefkes et al., 2008, 2010; Herz et al., 2014; Rehme et al., 2011; Rosch et al., 2018; Forrester et al., 2020; Singh et al., 2025). Effective connectivity, referring to the causal influences that different parts of the brain exert over each other, provides a direct understanding of the neural mechanisms underlying various cognitive processes in the brain. Instead of modelling individual neurons, DCM describes the average behaviour of neural populations. In particular, allowing for dynamic causal interactions between distinct brain regions, DCM can reveal biophysics-informed links between microscopic neural activity and macroscopic brain phenomena. By adjusting model parameters, researchers can simulate the transition from normal brain rhythms to pathological states, providing valuable insights into disease mechanisms and potential treatment strategies (Wendling et al., 2024; Friston et al., 2019). Sotero et al. (2007) used neural circuits to simulate EEG signals, helping to elucidate how the macroscopic electrical activity recorded from the scalp emerges from underlying neural dynamics. Using the DCM approach, Papadopoulou et al. (2015) tracked slow modulations in synaptic gain for a cohort of epileptic patients. Chen et al. (2009) employed spectral DCM on MEG scans to infer functional asymmetries in inter- and cross-frequency-coupling between brain regions during the period that subjects visually process faces. This approach can be used to model brain activity on a whole brain scale. With the Human Connectome Project dataset, Singh et al. (2025) developed a large scale, data-driven mean field cortical model for activities in the brain, involving hundreds of interacting neural populations.

Following Friston et al. (2019), a multiple cortical column DCM can be described by the following set of neural mass stochastic differential equations:

$$d\mathbf{x}(t) = f(\mathbf{x}(t), \mathbf{u}(t); \boldsymbol{\theta}, \mathbf{K})dt + \Gamma(\boldsymbol{\theta})d\mathbf{w}(t), \quad \mathbf{x}(0) = \mathbf{x}_0; \quad y(t) = h(\mathbf{x}(t)), \quad (1)$$

where  $\mathbf{w}(t)$  is a multivariate Gaussian white noise process,  $\mathbf{x}(t)$  is a vector of  $p$  hidden states,  $\mathbf{x}_0$  contains initial values of states,  $y(t)$  is the partial observation of hidden states,  $\mathbf{u}(t)$  is an external input,  $f$  is a nonlinear vector field,  $h$  is a function from  $\mathbb{R}^p \rightarrow \mathbb{R}$  with  $\boldsymbol{\theta}$  being a vector of local node parameters,  $\mathbf{K}$  a matrix of connection parameters between nodes,  $\Gamma(\boldsymbol{\theta})$  is a degenerate diffusion coefficient matrix. In the past two decades, considerable progress has been made in the development of dynamic causal modelling (Friston et al., 2019; Park et al., 2021; Forrester et al., 2020; Singh et al., 2025), and references therein. Despite this, a brain-wide search for dynamic causal abnormalities across spatial scales remains difficult, partly because of the challenges in modelling neural connectivities at large scale.

The first challenge is about how to solve and sample from nonlinear neural mass differential equations when the parameters involved are only partially identifiable. The following bilinear approximation of the equations is often used in the literature e.g., (Friston et al., 2003; Forrester et al., 2020) :

$$\begin{aligned} d\mathbf{x}(t) &\approx [f(\mathbf{x}_0, 0; \boldsymbol{\theta}, \mathbf{K}) + (\mathbf{A} + \mathbf{u}^T(t)\mathbf{B})\mathbf{x}(t) + \mathbf{C}\mathbf{u}(t)] dt + \Gamma(\boldsymbol{\theta})d\mathbf{w}(t), \\ \mathbf{x}(0) &= \mathbf{x}_0, \quad y(t) = h(\mathbf{x}(t)), \end{aligned}$$

where  $\mathbf{A} = \frac{\partial f}{\partial \mathbf{x}}|_{\mathbf{u}=0, \mathbf{x}=\mathbf{x}_0}$ ,  $\mathbf{B} = \frac{\partial^2 f}{\partial \mathbf{x} \partial \mathbf{u}}|_{\mathbf{u}=0, \mathbf{x}=\mathbf{x}_0}$  and  $\mathbf{C} = \frac{\partial f}{\partial \mathbf{u}}|_{\mathbf{u}=0, \mathbf{x}=\mathbf{x}_0}$ . This approximation is followed by a variational Bayesian analysis in order to select an optimal dynamic causal model from a list of pre-specified candidates.

Although the bilinear approximation can capture some parts of input-state interactions in the model (1), its accuracy deteriorates when strongly nonlinear regimes are introduced by spiking, bifurcations and saturation.

Instead, Kulik et al. (2023) used a fourth order stochastic Runge-Kutta method to numerically solve the coupled differential equations involved in the Jansen-Rit model. In these situations, recomputing the Jacobian-updating integrator continuously is required to solve the equations, making the computation infeasible when fitting many pairwise coupled DCMs to the data. On the other hand, a Chen-Fliess expansion (Chen, 1954; Fliess, 1981) can solve the above differential equations without using any approximation of the nonlinear vector fields. However, it still remains difficult to perform a Bayesian data analysis when the vector fields are highly nonlinear.

The second challenge is that some states  $\mathbf{x}(t)$  are only partially observed at discrete time points. Then the exact likelihoods for the transition densities are difficult to trace. To estimate these likelihoods, Pokern et al. (2009) proposed a data-augmentation algorithm to impute the hidden states. The computation was intensive and it did not always converge to the true values when many local hypoelliptic diffusions were included.

The third challenge is about how to implement large scale dynamic causal models, subject to a limited resource of computation (e.g., Honey et al., 2007; Li et al., 2020; Rosch et al., 2018; Singh et al., 2025). To reduce the model dimension, Forrester et al. (2020) made a very restrictive assumption that the cortical columns are homogeneous in the sense that the column parameters are kept the same across the columns.

The fourth challenge is about heterogeneity of human brains even when case and control subjects are matched by ages and genders (Zhang and Green, 2025; Li et al., 2025). It is unclear how to take individual brain differences into account in a dynamic causal model with M/EEG data. Finally, although the excitation-inhibition imbalance across columns has been shown to underlie an epileptic form of brain activity ( e.g., Friston et al., 2016), it is unclear how such a spatial distribution pattern is associated with epilepsy.

Here, to address these challenges, we first develop an EEG data-driven network of conditionally coupled dynamic causal models (NccDCM) across multiple cortical regions for cases and controls respectively, where each node corresponds to a functional unit that can be represented by a neural mass model, and with edges informed by effective connectivity. For simplicity, neural mass activities are described by stochastic Jansen-Rit models (Jansen and Rit, 1995; Ableidinger et al., 2017; Forrester et al., 2020).

We then calculate differential causal nets between cases and controls to quantify abnormal causality in patients. By these nets, we are able to identify intrinsic and extrinsic dynamic connectivity patterns that are associated with brain diseases. In the proposed network, each node describes a channel of neuron populations which may receive input signals from other channels. The strengths of directed connectivity between nodes are regularised by biophysics-informed parameters.

---

The above network structure allows for the nesting of sub-networks within a composite network, where the followed differential analysis of brain systems at different levels of detail can be based. The following assumptions are made in the NccDCM: Within each channel/node, the neurons can be modelled by three populations, namely, pyramidal cells (PCs), excitatory interneurons (EINs) and inhibitory interneurons (IINs), forming two feedback loops- a fast excitatory feedback loop with external input from paired opposite regions as well as an input of rough path noise from background; a slow inhibitory feedback loop. The output represents the membrane potential of pyramidal neurons, which are signals measured by the EEG device. The coupling within a node and between nodes are regularised by structural parameters. However, it should be noted that the precise nature of the within channel model is not restrictive and more complex models can be incorporated.

A conditional inference of the proposed model is implemented as follows: We first estimate NccDCMs by ccDCM screening, followed by inferring disease-associated causal nets from estimated contrasts between case and control subjects. The conditional estimation is carried out through minimising a profiled loss function based on what is called Chen-Fliess expansions of stochastic differential equations (Ableidinger et al., 2017; Chen, 1954; Fliess, 1981; Lyons, 1998). In the Chen-Fliess expansions, we solve the stochastic differential equations by linear combinations of iterative integrals of the vector of field functions. These estimated ccDCMs are then assembled via a post analysis of variance (Anderson, 2017). Unlike the existing approaches, which assume parameters to be known from diffusion-imaging data and previous literature (e.g., Forrester et al., 2020), we directly estimate local parameters in each node conditionally on inputs from other nodes by using subject's EEG data. This enables the inference of the large number of node parameters feasible even when nodes are heterogeneous. The estimated NccDCM allows us to investigate how neural activities in these channels/nodes influence each other, particularly, when defected channels/nodes exhibit pathological dynamics compared to healthy controls. Changes in these parameters reflect alterations in the balance between excitation and inhibition, compensatory adaption to abnormal inputs. We evaluate the proposed methodology on both simulated data and a recently published benchmark dataset of scalp EEG recordings for a group of pediatric epilepsy patients and their controls (OK et al., 2021). See Figure 9(a) for an example of interictal epileptiform discharges (IEDs) in the data and the bifurcation behaviour of the fitted ccDCM. In the real data analysis, we treat IEDs as electroencephalographic markers for epilepsy. IEDs reflect transient cortical hyperexcitability in neuron populations and are useful biomarkers in diagnosis and treatment of epilepsy. We are in particular interested in characterising the IED associated epileptic networks via differential dynamic causal nets, which shed light on the mechanisms of seizure propagation in brain regions.

The contributions of this paper are two-fold. First, we develop a novel network architecture that leverage the channel-wise coupling across a whole brain via hierarchical mixed-effects modelling. We provide a conditional inference scheme to estimate NccDCM. By the post analysis of variance, we demonstrate that the proposed modelling is promising in discovering novel differential dynamic causal nets and in providing a deep insight into abnormal connectivity in case subjects compared to healthy controls. Secondly, fitting the proposed NccDCM to an epileptic case-control dataset, we identify comprehensive neuronal circuits for a whole brain and reveal biophysics-informed dynamic causal nets that underlie defected brain connectivity in epileptic patients.

The remaining paper is organised as follows. The details of the proposed methodology and optimisation algorithm are provided in Section 2. The applications of the proposed methods to the IED dataset and synthetic data are presented in Section 3. Discussion and conclusions are made in Section 4.

---

## 2 Methodology

In this section, we consider a network of conditionally coupled dynamic causal models (ccDCMs) for cases and controls respectively. By conditionally coupling, we treat the output of each channel as a response in turn, neural populations within the channel as internal regressors and neural populations in outside channels as external regressors. We also assume that the model parameters for subjects in case/control group follow a mixed-effects model, accounting for group and subject-specific variations. The ccDCM of each node is then estimated by minimising an estimated loss function (i.e., minus twice estimated log-predictive-likelihood) based on an evolutionary optimisation algorithm. The loss function is constructed by use of the Chen-Fliess expansion.

We identify differential causal nets that differ cases from controls through post multivariate analysis of variance based on a package of permutational multivariate analysis of variance (Anderson, 2017).

### 2.1 Model and estimation

#### 2.1.1 NccDCM

Suppose that there are  $N_k$  subjects in groups  $k$ ,  $k = 0, 1$ . Each subject is scanned by an EEG device of  $J$  channels over time interval  $[0, T]$ . For each subject, outputs from channels are divided into segments over  $Q$  disconnected time periods. In the epilepsy study, these time-periods are referred to as seizure periods or pre-seizure periods. Let  $x_{0nq}^{(i)k}, x_{1nq}^{(i)k}$  and  $x_{2nq}^{(i)k}$  denote the states of the three neuronal populations, namely, pyramidal cells, excitatory interneurons and inhibitory interneurons in channel  $i$  for subject  $n$  in group  $k$ . These states can be described by three second-order ordinary differential equations that model modulations in the mean membrane potential due to the mean incoming firing rate from the same population and from other populations in the neural mass. The incoming mean firing rates are activated through a sigmoid transformation. These three equations are often re-expressed as six first order differential equations. Let  $y_{nq}^{(i)k}(t) = x_{1nq}^{(i)k}(t) - x_{2nq}^{(i)k}(t)$  denote the output of channel  $i$  in period  $q$  for subject  $n$  in group  $k$ .

To account for multiple nested sources of variability in the grouping subject data, the NccDCM, taking channels as nodes, is structured in a hierarchical regression manner: The node and edge parameters, differing between subjects, follow a mixed-effects model. Under the assumption of node homogeneity, Forrester et al. (2020) described the evolution of these state variables by  $J$  sets of six-dimensional stochastic differential equations:

$$\begin{aligned} dx_{0nq}^{(i)k}(t) &= x_{3nq}^{(i)k}(t) dt, \quad dx_{1nq}^{(i)k}(t) = x_{4nq}^{(i)k}(t) dt, \quad dx_{2nq}^{(i)k}(t) = x_{5nq}^{(i)k}(t) dt, \\ dx_{3nq}^{(i)k}(t) &= \left[ A_{nq}^k a S_{nq}^k \left( y_{nq}^{(i)k}(t) \right) - 2a x_{3nq}^{(i)k}(t) - a^2 x_{0nq}^{(i)k}(t) \right] dt, \\ dx_{4nq}^{(i)k}(t) &= \left\{ A_{nq}^k a \left[ K_{nq}^{(i)j)k} S_{nq}^k \left( y_{nq}^{(j)k}(t) \right) + C_{2nq}^k S_{nq}^k \left( C_{1nq}^k x_{0nq}^{(i)k}(t) \right) \right] \right. \\ &\quad \left. - 2a x_{4nq}^{(i)k}(t) - a^2 x_{1nq}^{(i)k}(t) \right\} dt + A_{nq}^k ad\tilde{\mathbf{w}}_{nq}^{(i)k}(t), \\ dx_{5nq}^{(i)k}(t) &= \left[ B_{nq}^k b C_{4nq}^k S_{nq}^k \left( C_{3nq}^k x_{0nq}^{(i)k}(t) \right) - 2b x_{5nq}^{(i)k}(t) - b^2 x_{2nq}^{(i)k}(t) \right] dt. \end{aligned}$$

$$i = 1, 2, \dots, J.$$

In node  $i$ , period  $q$  for subject  $n$  in group  $k$ , the error term is of form

$$d\tilde{\mathbf{w}}_{nq}^{(i)k}(t) = \left[ P^{(i)} + \sum_{j_1 \neq i, j} K_{nq}^{(i)j_1)k} S_{nq}^k \left( y_{nq}^{(j_1)k}(t) \right) \right] dt + d\mathbf{w}_{nq}^{(i)k}(t),$$

where  $\mathbf{w}_{nq}^{(i)k}(t)$  is a Gaussian noise process,  $P^{(i)}$  is a basal extracortical input,  $S_{nq}^k(\cdot)$  is a sigmoid function, the parameters  $A_{nq}^k$  and  $B_{nq}^k$  stand for the excitatory and inhibitory synaptic gains, the coupling parameters  $C_{mnq}^k, m = 1, 2, 3, 4$  represent the average numbers of synaptic connections between populations in each channel, and  $a^{-1}$  and  $b^{-1}$  are time constants. For  $1 \leq i \leq J$  in turn, fixing the parameters in nodes except the  $i$ -th, we solve the  $i$ -th set of stochastic differential equations.

In the following, we further remove the node-homogeneity assumption, allowing the node parameters to vary across nodes. For nodes  $1 \leq i \neq j \leq J$  and for subject  $n$  in group  $k$ , we define sigmoid function

$$S_{nq}^{(i|j)k}(x(t)) = \frac{\nu_{\max}}{1 + \exp(r(\nu_{0nq}^{(i|j)k} - x(t)))}, \quad t \in [0, T],$$

which activates input  $x(t)$ . Here,  $\nu_{\max}$  stands for the maximum firing rate of the neuron population,  $\nu_{0nq}^{(i|j)k}$  is the value for which a 50% of the maximum firing rate is attained by neurons in channel  $i$ , and  $r > 0$  is the slope of the above function at  $\nu_{0nq}^{(i|j)k}$ . At dendritic spines, incoming spikes are converted into postsynaptic potentials (PSPs) through convolution with an alpha-type response function (Bastiaens et al., 2024). PSPs are then converted into an average firing rate at the axon hillock using the above sigmoid function. Following Ableidinger et al. (2017), we model the three neuron populations in the channel  $i$ , when there is a signal transmission from the channel  $j$  to channel  $i$  with rate  $K_{nq}^{(i|j)k}$ , by the following stochastic Jansen-Rit differential equations:

$$\begin{aligned} dx_{0nq}^{(i)k}(t) &= x_{3nq}^{(i)k}(t) dt, \quad dx_{1nq}^{(i)k}(t) = x_{4nq}^{(i)k}(t) dt, \quad dx_{2nq}^{(i)k}(t) = x_{5nq}^{(i)k}(t) dt, \\ dx_{3nq}^{(i)k}(t) &= \left[ A_{nq}^{(i|j)k} a S_{nq}^{(i|j)k} \left( y_{nq}^{(i)k}(t) \right) - 2a x_{3nq}^{(i)k}(t) - a^2 x_{0nq}^{(i)k}(t) \right] dt, \\ dx_{4nq}^{(i)k}(t) &= \left\{ A_{nq}^{(i|j)k} a \left[ K_{nq}^{(i|j)k} S_{nq}^{(i|j)k} \left( y_{nq}^{(j)k}(t) \right) + C_{2nq}^{(i|j)k} S_{nq}^{(i|j)k} \left( C_{1nq}^{(i|j)k} x_{0nq}^{(i)k}(t) \right) \right] \right. \\ &\quad \left. - 2a x_{4nq}^{(i)k}(t) - a^2 x_{1nq}^{(i)k}(t) \right\} dt + A_{nq}^{(i|j)k} a d\tilde{\mathbf{w}}_{nq}^{(i|j)k}(t), \\ dx_{5nq}^{(i)k}(t) &= \left[ B_{nq}^{(i|j)k} b C_{4nq}^{(i|j)k} S_{nq}^{(i|j)k} \left( C_{3nq}^{(i|j)k} x_{0nq}^{(i)k}(t) \right) - 2b x_{5nq}^{(i)k}(t) - b^2 x_{2nq}^{(i)k}(t) \right] dt, \end{aligned} \quad (2)$$

where

$$d\tilde{\mathbf{w}}_{nq}^{(i|j)k}(t) = \left[ \sum_{j_1 \neq i, j} K_{nq}^{(i|j_1)k} S_{nq}^{(i|j_1)k} \left( y_{nq}^{(j_1)k}(t) \right) \right] dt + d\mathbf{w}_{nq}^{(i)k}(t),$$

given the external input from channel  $j$  and merging the inputs from other channels  $j_1 \neq i$  with the noise, the parameters  $A_{nq}^{(i|j)k}$  and  $B_{nq}^{(i|j)k}$  stand for the excitatory and inhibitory synaptic gains in channel  $i$  and period  $q$  for subject  $n$  in group  $k$  respectively, the coupling parameters  $C_{nq}^{(i|j)k}$  and  $C_{mnq}^{(i|j)k}, m = 1, 2, 3, 4$  represent the average numbers of synaptic connections between populations, and  $a^{-1}$  and  $b^{-1}$  are time constants. In light of Grimbert and Faugeras (2006), we set the ranges for these parameters in Table 1.

To summarise, in each ccDCM, three neural populations are described by six-dimensional stochastic differential equations. The three neural populations are interconnected through the coupling parameters in the equations, which determine the average evolution rates of the postsynaptic potential. The extrinsic parameter  $K_{nq}^{(i|j)k}$  regulates the influence of neural populations in channel  $j$  on the excitation of neural populations in channel  $i$  and thus determine the edge between nodes  $i$  and  $j$  in period  $q$  for subject  $n$  in group  $k$ . A large  $K_{nq}^{(i|j)k}$  increases the strength of neural synchronization, changing oscillatory activity or pathological dynamics such as epileptic discharges, while decreasing  $K_{nq}^{(i|j)k}$  reduces inter-regional coupling, giving rise to more

**Table 1.** Values of biophysical parameters in ccDCM.

Parameter	Description	Value
$A_{nq}^{(i j)k}$	Average excitatory synaptic gain	[2.6, 6] mV
$\theta_{nq2}^{(i j)k}$	Ratio of average excitatory-inhibitory synaptic gains	[0.05, 1]
$B_{nq}^{(i j)k}$	Average inhibitory synaptic gains	$A_{nq}^{(i j)k}/\theta_{nq2}^{(i j)k}$
$a^{-1}$	Time constant of excitatory postsynaptic potential	10 ms
$b^{-1}$	Time constant of inhibitory postsynaptic potential	20 ms
$A^{( j)k}C_{nq}^{(i j)k}$	Scaled avg. number of synapses between the populations	[0, 1000]
$C_{1nq}^{(i j)k}$	Avg. no. of syn. established by principal neurons on excitatory interneurons	$C_{nq}^{(i j)k}$
$C_{2nq}^{(i j)k}$	Avg. no. of syn. established by excitatory interneurons on principal neurons	0.8 $C_{nq}^{(i j)k}$
$C_{3nq}^{(i j)k}$	Avg. no. of syn. established by principal neurons on inhibitory interneurons	0.25 $C_{nq}^{(i j)k}$
$C_{4nq}^{(i j)k}$	Avg. no. of syn. established by inhibitory interneurons on principal neurons	0.25 $C_{nq}^{(i j)k}$
$A_{nq}^{(i j)k}K_{nq}^{(i j)k}$	Scaled edge from node $j$ to node $i$	[0, 700] mV
$v_{\max}$	Maximum firing rate of the neural populations	5 Hz
$v_{0nq}^{(i j)k}$	Value for which 50% of the maximum firing rate is attained	[0, 10] mV
$r$	Slope of the act. function at $v_{0nq}^{(i j)k}$	0.56 mV <sup>-1</sup>

localised dynamics. The above model supports oscillations that relate to input neural rhythms, such as the well-known, alpha, beta, and gamma brain rhythms, and also irregular, epileptic-like activity. It allows us to investigate how neural populations interact under both deterministic and stochastic settings, and how coupling between nodes modulates large-scale brain rhythms observed in E/MEG recordings (Forrester et al., 2020). As the nonlinear sigmoid function  $S_{nq}^{(i|j)k}$  is globally Lipschitz continuous, it follows from Theorem 6.2.2 of Arnold (1974) that the Eq. (2) has a path-wise unique and  $\mathcal{F}_t$ -adapted solution. We fix  $a$ ,  $b$ ,  $v_{\max}$  and  $r$  at their typical values as not all these parameters in the ccDCM are estimable. The architecture of NccDCM can be described by the following schematic diagram for five channels.

[Put Fig. 1 here.]

To facilitate the description of the nested links between subjects in different groups, we introduce more notations. Let  $\mathbf{A}_n^{(i|j)k} = (A_{n1}^{(i|j)k}, \dots, A_{nQ}^{(i|j)k})^T$ ,  $\mathbf{B}_n^{(i|j)k} = (B_{n1}^{(i|j)k}, \dots, B_{nQ}^{(i|j)k})^T$ ,  $\mathbf{C}_n^{(i|j)k} = (C_{n1}^{(i|j)k}, \dots, C_{nQ}^{(i|j)k})^T$ ,  $\mathbf{K}_n^{(i|j)k} = (K_{n1}^{(i|j)k}, \dots, K_{nQ}^{(i|j)k})^T$  and  $\boldsymbol{\nu}_{0n}^{(i|j)k} = (\nu_{0n1}^{(i|j)k}, \dots, \nu_{0nQ}^{(i|j)k})^T$  for subject  $n$  in group  $k = 0, 1$ , where  $1 \leq i \neq j \leq J$ , and  $1 \leq n \leq N_0$  for  $k = 0$  and  $1 \leq n \leq N_1$  for  $k = 1$ . Estimating these parameters depends on the external inputs as well as the internal self-inputs of each target-channel when we fit a ccDCM to the data. Note that the ccDCM is an ill-posed model and our simulations (see Section 3) show that the parameters  $\mathbf{A}_n^{(i|j)k}$  and  $\mathbf{B}_n^{(i|j)k}$  are not identifiable simultaneously. However, the ratio  $A_n^{(i|j)k}/B_n^{(i|j)k}$  can be estimated reasonably well. This motivates us to re-parameterise ccDCM by new parameters  $\boldsymbol{\theta}_{nq}^{(i|j)k} = (\theta_{nq1}^{(i|j)k}, \dots, \theta_{nq5}^{(i|j)k})^T = (A_{nq}^{(i|j)k}, A_{nq}^{(i|j)k}/B_{nq}^{(i|j)k}, A_{nq}^{(i|j)k} \times C_{nq}^{(i|j)k}, A_{nq}^{(i|j)k} \times K_{nq}^{(i|j)k}, \nu_{0nq}^{(i|j)k})^T$ . Putting these parameters together forms a vector, namely  $\boldsymbol{\theta}_{nq}^{(i|j)k} = (\boldsymbol{\theta}_{nqc}^{(i|j)k})$ . We assume that the above parameters follow the mixed-effects model

$$\boldsymbol{\theta}_{nqc}^{(i|j)k} = \boldsymbol{\delta}_{qc} + \boldsymbol{\alpha}_{qc}^{(k)} + \boldsymbol{\beta}_{qc}^{(i|j)} + c_{01} \boldsymbol{\alpha}_{qc}^{(k)} \odot \boldsymbol{\beta}_{qc}^{(i|j)} + \mathbf{r}_{nqc}^{(i|j)k}, \quad k = 0, 1; \quad q = 1, \dots, Q, \quad (3)$$

where  $\odot$  denotes the component-wise multiplication,  $\boldsymbol{\alpha}_{qc}^{(1)} + \boldsymbol{\alpha}_{qc}^{(2)} = 0$ ,  $\sum_{i \neq j} \boldsymbol{\beta}_{qc}^{(i|j)} = 0$ , and  $c_{01}$  is the coefficient satifying  $c_{01} \sum_q |\boldsymbol{\beta}_{qc}^{(i|j)} + 1| \neq 0$  and  $c_{01} \sum_q |\boldsymbol{\alpha}_{qc}^{(i|j)} + 1| \neq 0$ .

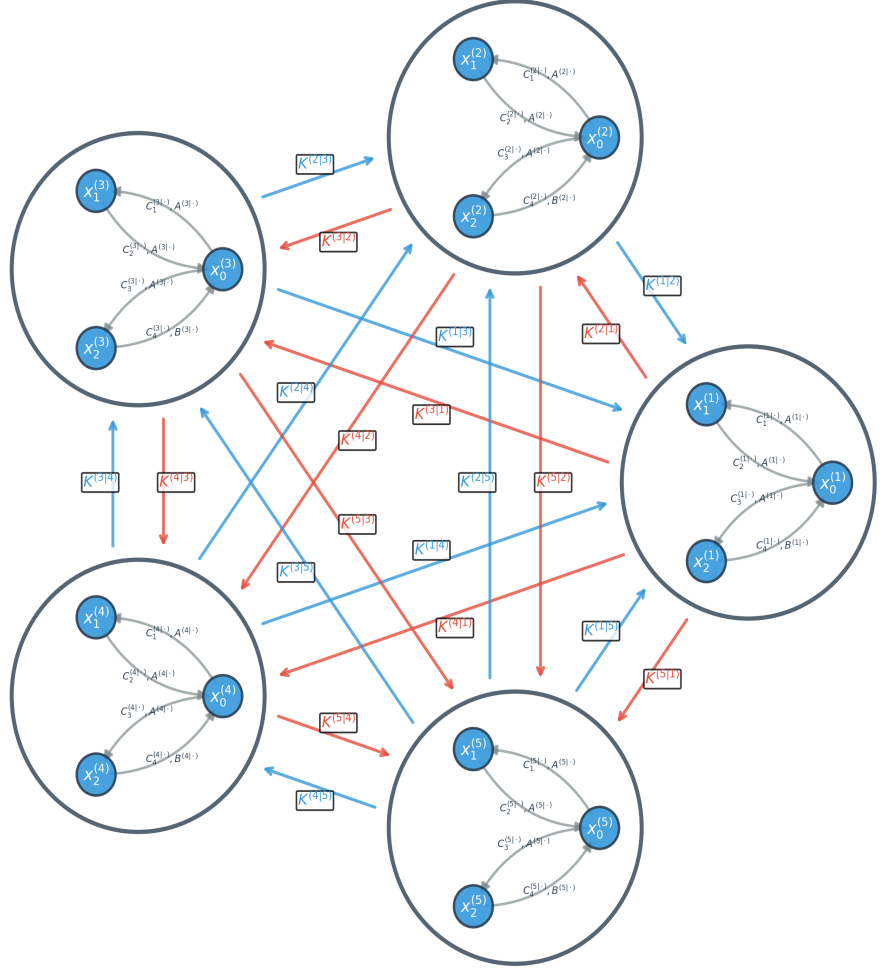


**Figure 1.** A schematic diagram of NccDCM of five channels. The bigger circles stand for channels, each described by a Jansen-Rit neural mass equation with the hidden states  $x_0$ ,  $x_1$ , and  $x_2$ . Parameters  $C^{(i|\cdot)}$ ,  $A^{(i|\cdot)}$ , and  $B^{(i|\cdot)}$  denote the within-channel parameters in channel  $i$ , taking into account the regressive effects of signal transmission from other channels. Parameter  $K^{(i|j)}$  defines a regressive coupling from a designated input channel  $j$  to output channel  $i$ .

### 2.1.2 Estimation

The estimation is implemented in three steps: First solve the Jansen-Rit neural mass differential equations, then construct the forward pairwise loss functions and finally minimising the loss functions by some evolutionary optimisation algorithms.

**Solving the Jansen-Rit neural mass differential equations.** To construct a loss function for estimation, we need to compute the forward solutions of the Jansen-Rit differential equations to predict the data points iteratively over a sequence of time-instances. We adopt the Chen-Fliess expansion, a linear combination of iterative Stratonovich integrals (Fliess, 1981), to solve the above Jansen-Rit input-output differential system.

For subject  $n$  in the group  $k$ , the EEG recordings in channel  $i$  over the  $q$ -th period are partitioned into  $D$  epochs, each contains  $b_q$  time-instants  $t_{0:b_q-1}^d = (t_0^d, \dots, t_{b_q-1}^d)$ , in the form  $\mathbf{Y}_{nq}^{(i)k}(t_{0:b_q-1}^d) = (y_{nq}^{(i)k}(t_0^d), y_{nq}^{(i)k}(t_1^d), \dots, y_{nq}^{(i)k}(t_{b_q-1}^d))$ ,  $d = 1, 2, \dots, D$ . Let  $x_{snq}^{(i)k}(t)$ ,  $s = 0, 1, 2$  denote the corresponding three hidden neural states. Let  $-\{3\} = \{0, 1, 2, 4, 5\}$ ,  $-\{1, 4\} = \{0, 2, 3, 5\}$  and  $x_{Inq}^{(i)k}(t) = (x_{snq}^{(i)k}(t))_{s \in I}$ . Denote the truncated Chen-Fliess expansions of the conditional expectations of  $y_{nq}^{(i)k}(t)$  and  $x_{snq}^{(i)k}(t)$ ,  $s = 0, 2, 3, 5$ , given by the forms

$$\begin{aligned} y_{nq}^{(i)k}(t_m^d) &\approx g\left(t_m^d | x_{-\{3\}nq}^{(i)k}(t_0^d), y_{nq}^{(i)k}(t_0^d), \dot{y}_{nq}^{(i)k}(t_0^d), y_{nq}^{(j)k}(t_0^d), \boldsymbol{\theta}_{nq}^{(i|j)k}\right), \\ x_{0nq}^{(i)k}(t_0^d) &\approx g_0\left(t_{b_q-1}^{d-1} | x_{\{0,3\}nq}^{(i)k}(t_0^{d-1}), y_{nq}^{(i)k}(t_0^{d-1}), \dot{y}_{nq}^{(i)k}(t_0^{d-1}), \boldsymbol{\theta}_{nq}^{(i|j)k}\right), \\ x_{2nq}^{(i)k}(t_0^d) &\approx g_2\left(t_{b_q-1}^{d-1} | x_{\{1,4\}nq}^{(i)k}(t_0^{d-1}), \boldsymbol{\theta}_{nq}^{(i|j)k}\right), \\ x_{3nq}^{(i)k}(t_0^d) &\approx g_3\left(t_{b_q-1}^{d-1} | x_{\{0,3\}nq}^{(i)k}(t_0^{d-1}), y_{nq}^{(i)k}(t_0^{d-1}), \dot{y}_{nq}^{(i)k}(t_0^{d-1}), \boldsymbol{\theta}_{nq}^{(i|j)k}\right), \\ x_{5nq}^{(i)k}(t_0^d) &\approx g_5\left(t_{b_q-1}^{d-1} | x_{\{1,4\}nq}^{(i)k}(t_0^{d-1}), \boldsymbol{\theta}_{nq}^{(i|j)k}\right), \end{aligned} \quad (4)$$

where  $g(t|\cdot)$ ,  $g_0(t|\cdot)$ ,  $g_2(t|\cdot)$ ,  $g_3(t|\cdot)$  and  $g_5(t|\cdot)$  are defined in the Appendix A. Then the truncated Chen-Fliess expansions of the above Jansen-Rit differential system can be written as a conditionally deterministic function, say  $g$  or  $g_m$ , plus a stochastic error term. Moreover, in the expansions of  $x_{0nq}^{(i)k}$ ,  $x_{2nq}^{(i)k}(t)$ , the stochastic error terms, only appearing in the terms of orders larger than 3, are bounded by  $|o_p((t - t_0)^4)|$ , while in the expansion of  $y_{nq}^{(i)k}(t)$ , the stochastic terms, not appearing in the term of order 1, is of the form  $A_{nq}^{(i|j)k} a \int_{t_0}^t (t - s) d\tilde{w}_{nq}^{(i)k}(s) + o_p((t - t_0)^3)$ . Therefore, these approximate functions of the conditional expectations in (4) provide the best one-step predictions of  $y_{nq}^{(i)k}(t)$  and  $x_{snq}^{(i)k}(t)$ .

**Constructing forward pairwise loss functions.** Let  $t_0^d = t_{b_q-1}^{d-1}$  and initiate  $x_{-\{1,4\}nq}^{(i)k}(t_0^1) = (0, \dots, 0)$ . Given the observed  $D$  epoch data, we can iteratively make one-step forward predictions of the hidden states and the channel outputs over time-grids by using the truncated Chen-Fliess expansions and the difference operator as follows: For the first epoch,

$$\begin{aligned} \dot{y}_{nq}^{(i)k}(t_0^1) &\approx (y_{nq}^{(i)k}(t_1^1) - y_{nq}^{(i)k}(t_0^1)) / (t_1^1 - t_0^1), \\ \hat{y}_{nq}^{(i)k}(t_m^1) &\approx g\left(t_m^1 | x_{-\{3\}nq}^{(i)k}(t_0^1), y_{nq}^{(i)k}(t_0^1), \dot{y}_{nq}^{(i)k}(t_0^1), y_{nq}^{(j)k}(t_0^1), \boldsymbol{\theta}_{nq}^{(i|j)k}\right), \end{aligned}$$

where  $x_{\{0:5\}nq}^{(i)k}(t_0^1) = (0, y_{nq}^{(i)k}(t_0^1), 0, 0, \dot{y}_{nq}^{(i)k}(t_0^1), 0)^T$ . In general, for  $m = 1, \dots, b_q - 1$  and  $d = 2, \dots, D$ ,

$$\begin{aligned}
\dot{y}_{nq}^{(i)k}(t_0^d) &\approx (y_{nq}^{(i)k}(t_1^d) - y_{nq}^{(i)k}(t_0^d))/(t_1^d - t_0^d), \\
\widehat{y}_{nq}^{(i)k}(t_m^d) &\approx g\left(t_m^d | x_{\{3\}nq}^{(i)k}(t_0^d), y_{nq}^{(i)k}(t_0^d), \dot{y}_{nq}^{(i)k}(t_0^d), y_{nq}^{(j)k}(t_0^d), \boldsymbol{\theta}_{nq}^{(i|j)k}\right), \\
\widehat{x}_{0nq}^{(i)k}(t_0^d) &\approx g_0\left(t_{b_q-1}^{d-1} | x_{\{0,3\}nq}^{(i)k}(t_0^{d-1}), y_{nq}^{(i)k}(t_0^{d-1}), \dot{y}_{nq}^{(i)k}(t_0^{d-1}), \boldsymbol{\theta}_{nq}^{(i|j)k}\right), \\
\widehat{x}_{2nq}^{(i)k}(t_0^d) &\approx g_2\left(t_{b_q-1}^{d-1} | x_{\{1,4\}nq}^{(i)k}(t_0^{d-1}), \boldsymbol{\theta}_{nq}^{(i|j)k}\right), \\
\widehat{x}_{1nq}^{(i)k}(t_0^d) &= y_{nq}^{(i)k}(t_0^d) + \widehat{x}_{2nq}^{(i)k}(t_0^d), \\
\widehat{x}_{3nq}^{(i)k}(t_0^d) &\approx g_3\left(t_{b_q-1}^{d-1} | x_{\{0,3\}nq}^{(i)k}(t_0^{d-1}), y_{nq}^{(i)k}(t_0^{d-1}), \dot{y}_{nq}^{(i)k}(t_0^{d-1}), \boldsymbol{\theta}_{nq}^{(i|j)k}\right), \\
\widehat{x}_{5nq}^{(i)k}(t_0^d) &\approx g_5\left(t_{b_q-1}^{d-1} | x_{\{1,4\}nq}^{(i)k}(t_0^{d-1}), \boldsymbol{\theta}_{nq}^{(i|j)k}\right), \\
\widehat{x}_{4nq}^{(i)k}(t_0^d) &= \dot{y}_{nq}^{(i)k}(t_0^d) + \widehat{x}_{5nq}^{(i)k}(t_0^d).
\end{aligned}$$

We construct a forward pairwise loss function by the summation of the squared prediction errors over the set of increasing time-instances  $T_q = \{t_0^1, \dots, t_{b_q-1}^1; \dots; t_0^D, \dots, t_{b_q-1}^D\}$ . These time-instances are generated by concatenating time-instances in epochs. For the subject  $n$  in group  $k$ , the resulting loss function in the channel  $i$ , with a regressive input from the channel  $j$ , can be written as

$$L_{nq}^{(i|j)k}(\boldsymbol{\theta}_{nq}^{(i|j)k}) = \sum_{t \in T_q} \left( y_{nq}^{(i)}(t) - \widehat{y}_{nq}^{(i)k}(t) \right)^2.$$

Minimising the above loss function with respect to parameters  $\boldsymbol{\theta}_{nq}^{(i|j)k}$ , we obtain the estimate  $\widehat{\boldsymbol{\theta}}_{nq}^{(i|j)k}$ .

**Solving the optimisation problem.** Note that the above non-convex loss function contains multiple local minima as only partial observations on hidden states are available in dynamic causal modelling. We employ a genetic evolutionary algorithm of Zhang and Sanderson (2009), called adaptive differential evolution with optional external archive (JADE), to search for global minima. JADE evolves a population of candidate solutions through mutation, crossover, and selection, aiming to explore the landscape of the loss function around a global minimum. See the Appendix Sa, the Supplementary Material for the further details of the JADE.

## 2.2 Identify differential causal nets via mixed-effects modelling

Having obtained estimated networks of ccDCMs for cases and controls respectively, we want to find differential causal nets by contrasting cases and controls in terms of the estimated within-channel parameters and the between-channel parameters respectively. In the differential causal net for the  $c$ -th component of the parameter, we assign a link that is directed from node  $j$  to node  $i$  if the estimated values  $(\widehat{\boldsymbol{\theta}}_{nqc}^{(i|j)1})_{1 \leq q \leq Q}, 1 \leq n \leq N_1$  in cases are significantly different from their counterparts in controls.

In order to test for the significant differences between cases and controls, we treat the case-control memberships and channel memberships as factors in the following two-factor mixed-effects model

$$\widehat{\boldsymbol{\theta}}_{nq}^{(i|j)k} = \boldsymbol{\delta}_q + \boldsymbol{\alpha}_q^{(k)} + \boldsymbol{\beta}_q^{(i|j)} + c_{01} \boldsymbol{\alpha}_q^{(k)} \odot \boldsymbol{\beta}_q^{(i|j)} + \boldsymbol{r}_{nq}^{(i|j)k}, \quad k = 0, 1; \quad q = 1, \dots, Q, \quad (5)$$

where  $\odot$  denotes the component-wise multiplication and we write each estimated parameter as the summation of a baseline, fixed-factors related to case-control memberships and channels, and subject-specific random factors. Here, the significance of the case-control factor implies that case-control memberships make a contribution to the group differences while the significance of the channel-factor show that the group difference should be accounted for by multiple channels. The significance of random-effects (e.g., the difference of the variations across groups) implies that subject-specific variations play a role in differencing the groups from each other.

To make the above model identifiable, we assume that  $\alpha_q^{(1)} + \alpha_q^{(2)} = 0$ ,  $\sum_{i \neq j} \beta_q^{(i|j)} = 0$ , and  $c_{01}$  is the coefficient satisfying  $c_{01} \sum_q |\beta_{qc}^{(i|j)} + 1| \neq 0$  and  $c_{01} \sum_q |\alpha_{qc}^{(i|j)} + 1| \neq 0$ . Under the assumption that the parameters for different subjects are independent of each other, the expected Manhattan distances between the groups and within the groups admit

$$\begin{aligned} E \sum_q |\theta_{nqc}^{(i|j)1} - \theta_{mqc}^{(i|j)0}| &= \sum_q E |r_{1qc}^{(i|j)0} - r_{1qc}^{(i|j)1}|, \\ E \sum_q |\theta_{nqc}^{(i|j)k} - \theta_{mqc}^{(i|j)k}| &= \sum_q E |\theta_{nqc}^{(i|j)k} - \theta_{mqc}^{(i|j)k}|, \quad k = 0, 1. \end{aligned} \quad (6)$$

Approximating the expectations in equation (6) by the U-statistics Lee (1990), we have the following statistics: For  $1 \leq c \leq 5$ ,  $k = 0, 1$ , and  $1 \leq i \neq j \leq J$ ,

$$\begin{aligned} \sigma_{cck}^{(i|j)} &= \frac{2}{N_k(N_k - 1)Q} \sum_{1 \leq m < n \leq N_k} \sum_{1 \leq q \leq Q} |\theta_{mqc}^{(i|j)k} - \theta_{nqc}^{(i|j)k}|, \\ \sigma_{c01}^{(i|j)} &= \frac{1}{N_0 N_1 Q} \sum_{1 \leq m \leq N_0, 1 \leq n \leq N_1} \sum_{1 \leq q \leq Q} |\theta_{mqc}^{(i|j)0} - \theta_{nqc}^{(i|j)1}|, \quad 1 \leq q \leq Q, \end{aligned}$$

which are the empirical versions of the within-group and between group average distances. For  $2 \leq c \leq 5$  (estimable parameters), to test the above null hypothesis  $H_0$ , we consider the test statistics  $\mathbf{F}^{(i|j)} = (F_1^{(i|j)}, \dots, F_5^{(i|j)})^T$  with

$$F_c^{(i|j)} = \frac{(N_0 + N_1)\sigma_{c01}^{(i|j)}}{N_0\sigma_{c00}^{(i|j)} + N_1\sigma_{c11}^{(i|j)}}.$$

We permuted the case-control memberships  $M$  times with default value  $M = 4999$ . For each permutation, we recomputed the value of  $F_c^{(i|j)}$ , obtaining  $M$  permuted  $F$ -values. The permuted p-values  $p_c$  is then defined by counting the proportion of the permuted  $F$ -values that are less than the observed value of  $F_c^{(i|j)}$ . We also run a permuted  $F$ -test for differences in the variances of the random factors of patients and controls. Similarly, we test the null hypothesis that  $\beta_{qc}^{(i|j)} = 0$  for all  $(i, j)$ .

### 2.3 Identifying differential causal nets between preictal and ictal periods

Understanding differences of epileptic patients between the preictal period and ictal period is crucial for gaining deeper insights into the mechanisms underlying epileptic seizures. While most studies focus on the ictal states, examining the transition from the preictal phase to the ictal phase can reveal early neural signatures that precede seizure onset. Identifying such signatures are important not only for elucidating pathophysiological dynamics of epilepsy but also for improving seizure prediction and thus developing early intervention strategies.

For each of parameters in  $(A_{nq}^{(i|j)k} / B_{nq}^{(i|j)k}, A_{nq}^{(i|j)k} * C_{nq}^{(i|j)k}, A_{nq}^{(i|j)k} * K_{nq}^{(i|j)k}, v_{0nq}^{(i|j)k})$  and for each channel pair, let  $\Pi_{\text{pre}}^{(\cdot)}$  and  $\Pi_{\text{on}}^{(\cdot)}$  denote the matrices of estimates derived from the NccDCM in the preictal and ictal periods respectively. Column of  $\Pi_{\text{pre}}^{(\cdot)}$  and  $\Pi_{\text{on}}^{(\cdot)}$  stand for the estimators of different case-subjects indexed by  $1 \leq n \leq N_1$  while rows correspond to different time segments indexed by  $1 \leq q \leq 6$ . We performed multiple permutation-based Wilcoxon signed-rank tests for significant NccDCM changes from the preictal period to the ictal period. They are implemented in four steps as follows:

- **Compute the test statistics**  $W = (W_1, W_2, \dots, W_{N_1})^\top$ . For subject  $n$ , denote the  $n$ -th columns of  $\Pi_{\text{pre}}^{(\cdot)}$  and  $\Pi_{\text{on}}^{(\cdot)}$  as  $\pi_{\text{pre}}^{(\cdot, n)}$  and  $\pi_{\text{on}}^{(\cdot, n)}$ , respectively. Compute the paired differences  $\pi_{\text{on}}^{(\cdot, n)} - \pi_{\text{pre}}^{(\cdot, n)}$ . After removing zero differences, rank the absolute values of the remaining differences in ascending order, assigning average ranks in the case of ties. The statistic  $W_n$  is then obtained by summing the ranks corresponding to positive differences, i.e., those instances where  $\pi_{\text{on}}^{(\cdot, n)} > \pi_{\text{pre}}^{(\cdot, n)}$ .
- **Pair-matched permutation procedure.** For each column in  $\Pi_{\text{pre}}^{(\cdot)}$ , find the corresponding column in  $\Pi_{\text{on}}^{(\cdot)}$ . We randomly swap the corresponding entries in the two columns, yielding  $2^6$  distinct permutations. For each permutation  $\alpha$ , we denote the resulted permuted matrices by  $\Pi_{\text{pre}}^{(\cdot, \alpha)}$  and  $\Pi_{\text{on}}^{(\cdot, \alpha)}$ .  $W^\alpha$  is reduced to the observed statistic  $W$  when  $\alpha$  is an identity permutation. The procedure is implemented as follows.
- **Compute the empirical  $p$ -values.** For the  $n$ -th subject, the empirical  $p$ -value is computed as

$$p^{(n)} = \frac{\#\{W_n^\alpha \geq W_n\}}{\text{Total number of permutations}},$$

where the numerator counts the number of permuted statistics at least as extreme as the observed  $W_n$ . This yields the individual  $p$ -value for each subject.

- **Combine the  $p$ -values using Fisher's method.** Combining these individual  $p$ -values using Fisher's method, we have the combined test statistic

$$\chi_{\text{Fisher}}^2 = -2 \sum_{n=1}^{N_1} \ln p^{(n)}.$$

The above statistic follows a chi-square distribution with  $2 \times N_1$  degrees of freedom under the null hypothesis that there are no changes in the parameters from the preictal period to the ictal period. The overall significance can be derived from the above chi-square distribution.

## 3 Results

We investigate the behavior of the proposed model and evaluate the performance of the proposed estimating method using simulated and real EEG data.

### 3.1 Differential causal nets between cases and controls

A healthy, balanced brain connectivity is critical for maintaining brain functions. In contrast, an abnormal brain connectivity can change subject's behavior by affecting certain areas involved in seizure propagation. Epilepsy is a group of neurological

---

disorders characterized by abnormal spontaneous brain activity, involving multiscale changes in brain functional organizations. The system epilepsy hypothesis posits that the enduring susceptibility to generate seizures in epilepsy is due to the specific vulnerability of the brain system (Fisher and et al., 2005). Abnormal firing of neurons causes defected local circuit function, leading to alterations of macroscale functional activities during seizure propagation (Burman and Parrish, 2018). The virtual brain model has demonstrated that a combination of a global shift in the brain's dynamic equilibrium and locally hyperexcitable network nodes provides a mechanistic explanation for the epileptic brain during interictal resting state (Courtial et al., 2020; Yang et al., 2024). Interictal Epileptiform Discharges (IEDs) in routine EEG recordings is crucial evidence of epilepsy in patients. OK et al. (2021) published a benchmark dataset for detecting IED. However, it is not clear to what extent the IEDs affect macroscale intrinsic dynamics and microcircuit organizations, that supports their pathological relevance. Here, we fit the NccDCM to this dataset to identify defected dynamic causal nets associated with the IED.

### 3.1.1 Description of case-control data

The above dataset contains EEG recordings in 18 EEG channels for 21 subjects who underwent EEG tests for epilepsy. Figure 2 in the Appendix Sc, the Supplementary Material shows a standard international 10 ~ 20 system for the electrode placement on the human scalp, used primarily in EEG. This system ensures standardized and reproducible positioning of electrodes across subjects and recording sessions based on precise anatomical landmarks. Longitudinal bipolar montage is used for channel configuration for the EEG recording, and the considered channels are FP2F4, F4C4, C4P4, P4O2, FP1F3, F3C3, C3P3, P3O1, FP2F8, F8T4, T4T6, T6O2, FP1F7, F7T3, T3T5, T5O1, FZCZ, CZPZ, and BP3REF (18 EEG channels and 1 ECG channel). See Table 1 in the Appendix Sc, the Supplementary Mateial for the brain regions which the electrode-pairs cover. Among these 21 subjects, IED time series were identified in the recordings of 11 subjects as confirmed by neurologists while the remaining 10 subjects were free from IEDs. Furthermore, for each of 8 patients, we were able to define 6 segments of IED time series, each of length 20 seconds, which were respectively matched by the segments of time series of 10 controls at the same time-periods. In the following analysis, we focus on these 8 patients against 10 controls. An example of the IED time series from the channel F4C4 of the control-subject H9 is displayed in Figure 12(a).

### 3.1.2 Subject-heterogeneity analysis

We began with a heterogeneity analysis for control-case groups using hierarchical clustering. We took the C3P3 channel as an example. The subject's EEG time series in the C3P3 and other channels were extracted from the same time period across all subjects. We calculated the feature vector of marginal mean, variance and the autocorrelations at the first 50 lags for each subject's EEG time series. Subject-heterogeneity in the C3P3 and other channels was assessed through hierarchical clustering of these feature vectors, where the Euclidean distance based average linkage method was adopted to generate dendograms. The results for the C3P3 and other channels, displayed in Figure 3 and the Appendix Se, showed evidence of subject-heterogeneity in the case and control groups. These findings gave us a rational to fit the NccDCM individually for each subject to capture subject-specific dynamics. This approach allowed us to make group-level inferences while accounting for individual variability through a mixed-effects model.

---

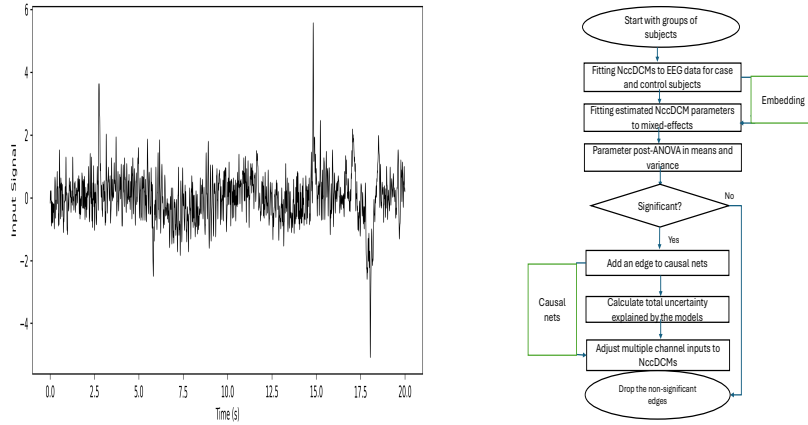


**Figure 2.** An example of the IED time series from the C3P3 channel of the patient P3 and the flowchart of the NccDCM analysis.

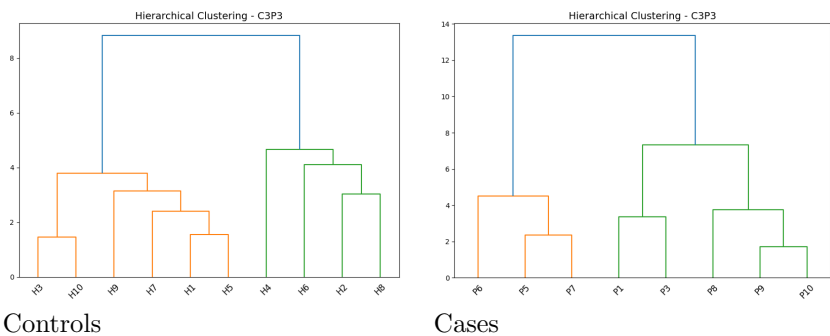


**Figure 3.** Dendrograms for clustering subjects based on the time series data derived from the channel C3P3 for the control and case groups.

### 3.1.3 Differential dynamic causal nets in means

For each pair of channels, we first fit ccDCMs to recorded patients' IED time series and their counterparts in controls respectively, obtaining the estimated values of parameters in the ccDCMs. We then perform a post-analysis of variance on these estimated parameters to reveal the IED-associated causal patterns in terms of channel excitation-inhibition ratio of synaptic gain, the strength of within-channel connectivity, the strength of between-channel connectivity and the contrasts of synaptic transmission between cases and controls during seizure periods.

For each of parameters  $A_{nq}^{(i|j)k}/B_{nq}^{(i|j)k}$ ,  $A_{nq}^{(i|j)k} * C_{nq}^{(i|j)k}$ ,  $A_{nq}^{(i|j)k} * K_{nq}^{(i|j)k}$ ,  $v_{0nq}^{(i|j)k}$  and each pair of channels  $(i, j)$ , we used the R software developed by Anderson (2017) to perform post analysis of variance to test whether there is a significant difference between case and control groups. The manhattan distance was used in these tests. To control the False Discovery Rate (FDR), the resulting  $p$ -values were further adjusted via the Benjamini-Hochberg method (Benjamini and Hochberg, 1995). Based on the adjusted  $(1 - p)$ -values, we constructed the adjacency matrix to reflect the degree of difference between the case and control groups. To facilitate the presentation, we retained only the values of  $(1 - p)$  that are larger than 95%. The resulting differential dynamic causal nets are displayed in Figure 4. In the nets, the directionality was indicated by arrows from an input channel to an output channel. The value of  $(1 - p)$  increased from 0.95 to 0.99 as colors are ranging from dark purple to yellow. From Figure 4, we revealed the following causal nets:

- $A_{nq}^{(i|j)k}/B_{nq}^{(i|j)k}$ : In Figure 4(a), there were 6 channel pairs to be claimed to differ cases from controls significantly: P4O2→FP1F7, T6O2→FP1F7, T5O1→FP1F7, C3P3→F7T3, C4P4→T6O2, and T5O1→T6O2.
- $A_{nq}^{(i|j)k} * C_{nq}^{(i|j)k}$ : In Figure 4 (b), there were 98 channel pairs to be found to have significant differences between cases and controls. Notably, these differences were most pronounced in channel pairs where prefrontal regions served as output channels, including FP1F7, FP1F3, FP2F8, FZCZ and FP2F4, corresponding to the left and right dorsolateral and ventrolateral prefrontal cortices. This finding highlighted the prominent role of these prefrontal areas in driving network-level alterations.
- $A_{nq}^{(i|j)k} * K_{nq}^{(i|j)k}$ : In Figure 4(c), 51 channel pairs of channels exhibited significant differences between cases and controls. These differences were predominantly observed in the frontal regions.
- $v_{0nq}^{(i|j)k}$ : In Figure 4(d), there were 121 channel pairs which showed significant differences between cases and controls. The most pronounced differences were in the prefrontal and central-temporal-parietal region, where FP1F7, FP1F3, C3P3, T3T5, P4O2 and T4T6 served as output channels.

In summary, for the parameters  $A_{nq}^{(i|j)k}/B_{nq}^{(i|j)k}$ ,  $A_{nq}^{(i|j)k} * C_{nq}^{(i|j)k}$ ,  $A_{nq}^{(i|j)k} * K_{nq}^{(i|j)k}$  and  $v_{0nq}^{(i|j)k}$ , the most pronounced differences between the case and control groups were in channel pairs with the output channels in the frontal regions. In particular, for  $A_{nq}^{(i|j)k} * K_{nq}^{(i|j)k}$ , the majority of significant channel pairs in frontal channels. For the parameter  $v_{0nq}^{(i|j)k}$ , significant differences between cases and controls were observed in nearly whole brain. An altered excitation/inhibition (E/I) balance, often involving decreased inhibition, has been identified as a robust biomarker in various neurodegenerative diseases such as Alzheimer's disease (AD) and frontotemporal dementia (FTD). Our analysis showed a mechanism that epilepsy shared with other

neurological diseases that changes in the inhibitory connections in the frontal cortex disrupted normal circuit operations and brain network dynamics.

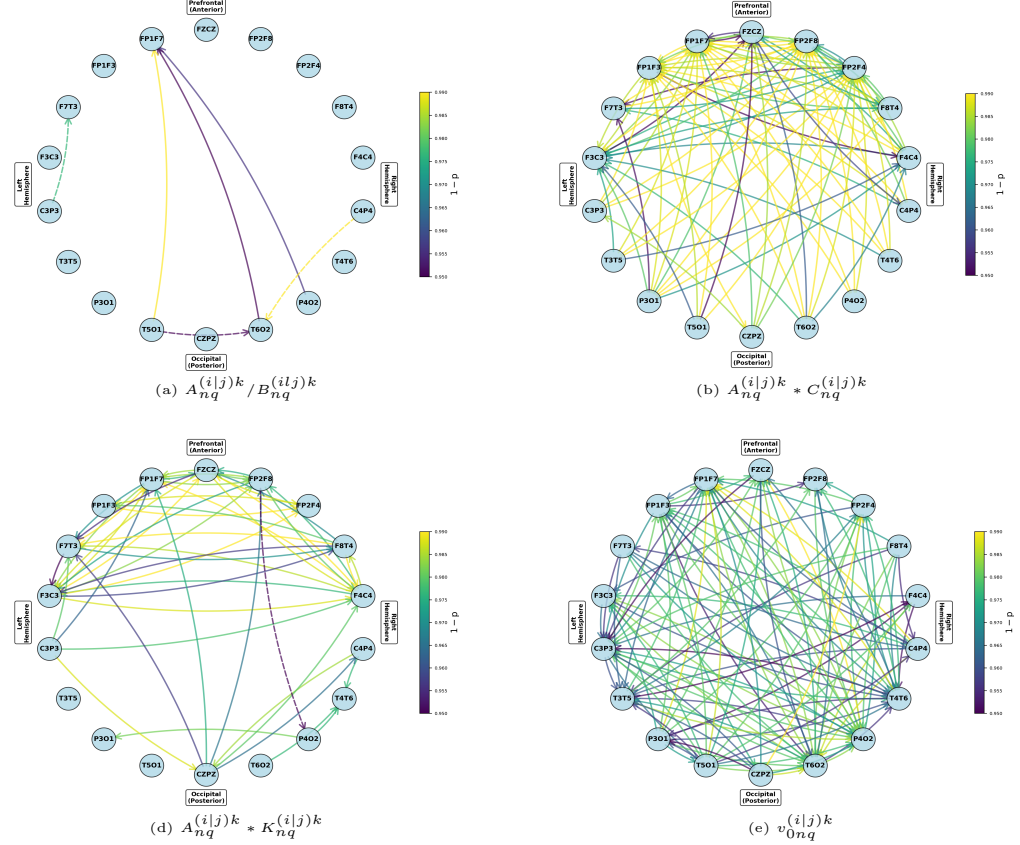


**Figure 4.** Networks for significant parameters changes after the corrections for multiple testing in the function of inhibitory connections (e.g., in the frontal cortex in psychosis) disrupt normal circuit operations and network dynamics.  $A_{nq}^{(i|j)k} / B_{nq}^{(ilj)k}$ ,  $A_{nq}^{(i|j)k} * C_{nq}^{(i|j)k}$ ,  $A_{nq}^{(i|j)k} * K_{nq}^{(i|j)k}$  and  $v_{0nq}^{(i|j)k}$ . Dashed lines stand for edges where the case mean is smaller than the control mean, while solid lines represent edges where the case mean is larger than the control mean.

### 3.1.4 Differential causal nets in variation

For each of parameters  $A_{nq}^{(i|j)k} / B_{nq}^{(ilj)k}$ ,  $A_{nq}^{(i|j)k} * C_{nq}^{(i|j)k}$ ,  $A_{nq}^{(i|j)k} * K_{nq}^{(i|j)k}$ , and  $v_{0nq}^{(i|j)k}$ , we employed the **betadisper** and **permute** functions in the R to conduct a test of multivariate homogeneity of group dispersions, thereby assessing whether the groups exhibited different variations across channels. As before, the distance matrix required in the software was derived from the manhattan method and the resulting  $p$ -values were adjusted for multiple testing. Based on the adjusted  $(1 - p)$ -values, we constructed the adjacency matrix to reflect the degree of difference between the case and control groups. We retained only the  $(1 - p)$  values exceeding 95% and otherwise set them to zeros. The results were displayed in Figure 4. In the differential causal nets, the directionality from an input channel to an output channel was indicated by arrows. As before, the value of  $(1 - p)$  increased from 0.95 to 0.99 as colors were changed from dark purple to yellow. The findings are summarized as follows:

- $A_{nq}^{(i|j)k} / B_{nq}^{(ilj)k}$ : From Figure 5(a), 14 channel pairs were identified as significantly

different between cases and controls. These differences were most pronounced in channel pairs with output channels in the prefrontal regions, including FP1F7, FP2F8 and FP1F3 in the left and right dorsolateral and ventrolateral prefrontal cortices.

- $A_{nq}^{(i|j)k} * C_{nq}^{(i|j)k}$ : From Figure 5(b), 9 channel pairs were found significantly different between cases and controls. These differences were predominantly observed in the frontal regions.
- $A_{nq}^{(i|j)k} * K_{nq}^{(i|j)k}$ : From Figure 5(c), 54 channel pairs exhibited significant differences between cases and controls. These differences were most located in channel pairs with output channels in the prefrontal regions. They included FP1F7, FP2F8, F4C4, F7T3, FZCZ, FP2F4 and FP1F3 in the left and right dorsolateral and ventrolateral prefrontal cortices.
- $v_{0nq}^{(i|j)k}$ : No significant differences were found between cases and controls for any channel pair of channels.

In summary, for the parameters  $A_{nq}^{(i|j)k} / B_{nq}^{(i|j)k}$ ,  $A_{nq}^{(i|j)k} * C_{nq}^{(i|j)k}$ , and  $A_{nq}^{(i|j)k} * K_{nq}^{(i|j)k}$ , the differences between cases and controls were most pronounced in channel pairs with the output channels in the frontal cortices.

### 3.1.5 Post ANOVA tables for the NccDCM

We treated the fitting of the NccDCM to each subject as a transformation of its EEG measurements into the values of the estimated network parameters, which inherited the uncertainty in the original data. We used the `adonis2` function in the R software to perform post multivariate ANOVA on these values and to test the significance of case-control and channels as two factors. The numerical results are displayed in Figure 6 and in Tables 2-5, the Appendix Sd, the Supplementary Material. The results indicated that the identified dynamic causal nets were highly significant for each parameter. The percentages of variations in the EEG data explained by the estimated dynamic causal nets, in terms of  $A_{nq}^{(i|j)k} / B_{nq}^{(i|j)k}$ ,  $A_{nq}^{(i|j)k} * C_{nq}^{(i|j)k}$ ,  $A_{nq}^{(i|j)k} * K_{nq}^{(i|j)k}$  and  $v_{0nq}^{(i|j)k}$  were 12%, 22%, 38% and 28% respectively. Here, the factor case-control occupied 1.7% (p-value 0.0002), 11.4% (p-value 0.0002), 7.4% (p-value 0.0002) and 18.4% (p-value 0.0002) respectively. The percentages of variations in the estimated parameters,  $R^2$  values confirmed the significant heterogeneity of the network parameters across the channels. For example, around 6% (p-value 0.035) of the variations in the estimated excitation/inhibition ratios was due to the channel difference.

### 3.1.6 Lagged correlation analysis

To compare with lagged correlation analysis, we calculated lagged correlation coefficients using the method in the Appendix Sb, the Supplementary Material. The analysis revealed 31 channel pairs with  $p$ -values less than 0.05 in testing the difference of lagged correlations between the control and case groups. See Figure 5(d) for the display. The channel pairs (FP2F4, P4O2), (FP2F4, F3C3), (F4C4, FP1F7), (FP1F3, F8T4), (F3C3, FP1F7), (F3C3, FZCZ), and (FP1F7, FZCZ) with  $p$ -values were smaller than 0.005. Among them, channel pairs (FP2F4, F3C3), (F4C4, FP1F7), (FP1F3, F8T4), and (F3C3, FP1F7) were also identified in the  $A_{nq}^{(i|j)k} * K_{nq}^{(i|j)k}$  based NccDCM analysis. However, unlike the previous NccDCM analysis, there were no significant pairs left at 5% after the Benjamini-Hochberg correction for multiple testing. This showed the advantages of the NccDCM analysis over the conventional correlation analysis.

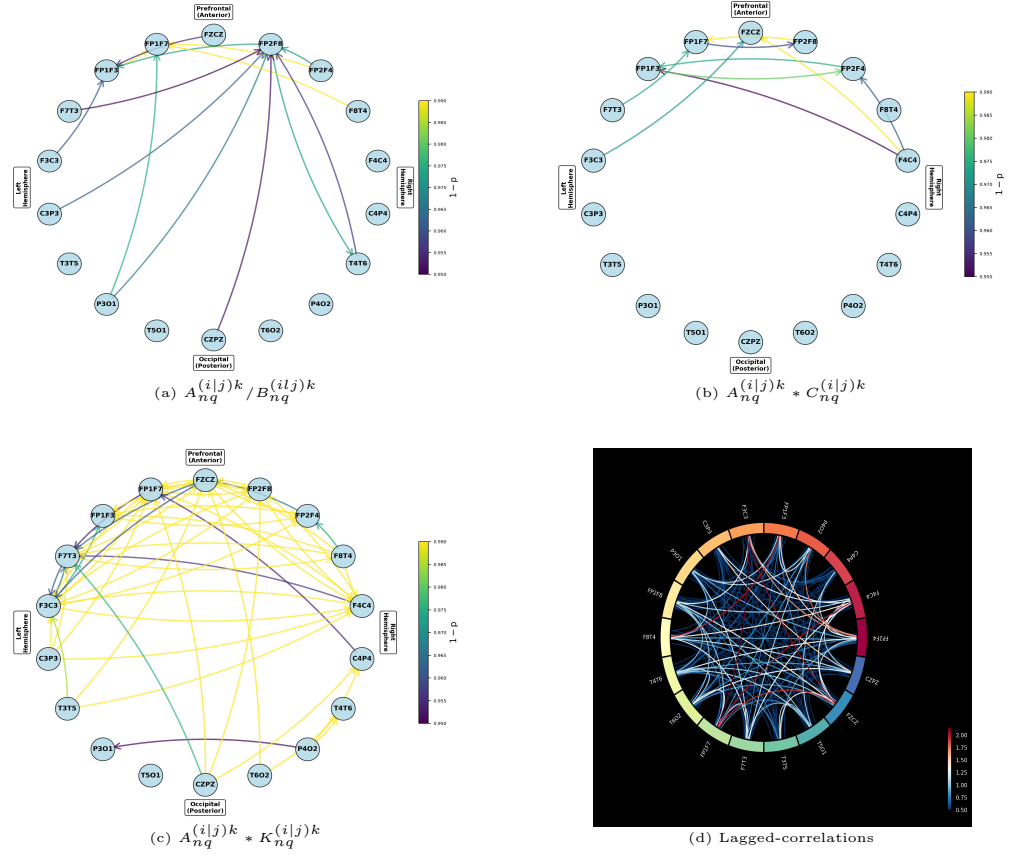


**Figure 5.** Differential causal nets in variation for parameters after the adjustments for multiple testing: (a)  $A_{nq}^{(i|j)k} / B_{nq}^{(i|j)k}$ , (b)  $A_{nq}^{(i|j)k} * C_{nq}^{(i|j)k}$  and (c)  $A_{nq}^{(i|j)k} * K_{nq}^{(i|j)k}$  in case-control groups. No significant differential causal nets in variation found in  $v_{0nq}^{(i|j)k}$ . By dashed (solid) lines, we meant the case mean of variation was smaller (larger) than the control mean of variation. For a comparison, the maximum lagged correlations-based functional connectivity was also plotted in (d). There were no significant lagged correlations left after the adjustments for multiple testing.

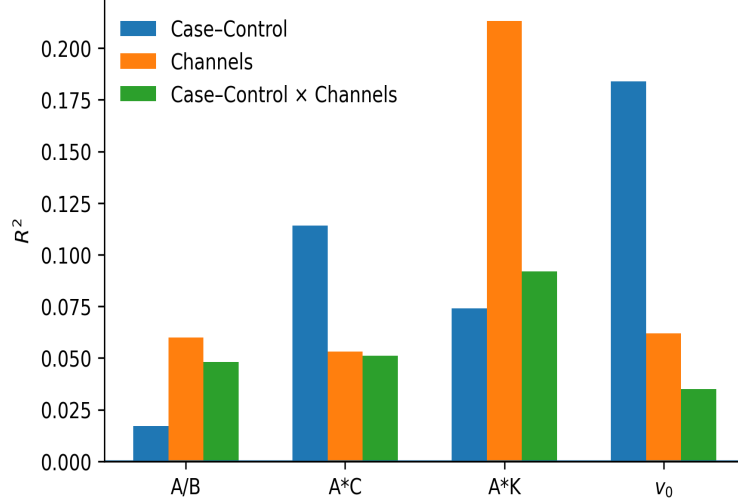


**Figure 6.** The percentages of uncertainty in the data which was explained by the NccDCM-based mixed-effects models,  $R^2$ . See Anderson (2017) for the definition of  $R^2$ .

### 3.2 Differential causal nets between preictal and ictal periods

**Description of pair-matched data** According to the annotations provided by OK et al. (2021), in the preictal periods, the epileptic subjects P1, P3 and P5~P9 were selected with six 20 seconds long preictal segments of time series identified. P2, P4 and P10 were excluded from further analysis as there were no six 20 seconds long preictal segments identified. Note that the preictal-ictal period dataset was period-matched for each subject while the case-control dataset was not pair-matched.

**Identified differential causal nets** . We fitted a NccDCM to the EEG recordings for each subject in the preictal period and the ictal period respectively, followed by the pair-matched post Wilcoxon signed rank test for the period differences. The results illustrated in Figure 7 suggest that, in patients with epilepsy, the NccDCM parameters exhibited noticeable increases from the preictal period to the ictal period. These changes were associated with seizure onset. However, there were no significant changes in these parameters to be found from the ictal period to the preictal period.

### 3.3 Simulation studies

#### 3.3.1 Properties of ccDCMs

As ccDCMs play a key role in shaping and influencing the structure and behavior of the NccDCM, in the following we exam the behavior of ccDCM and evaluate the accuracy of the proposed parameter estimation. For this purpose, suppressing channel and group subscripts in the model (2), consider the following ccDCM with states

$\mathbf{x}(t) = (x_0(t), x_1(t), x_2(t), x_3(t), x_4(t), x_5(t))$ :

$$\begin{aligned}
 dx_0(t) &= x_3(t)dt, \quad dx_1(t) = x_4(t)dt, \quad dx_2(t) = x_5(t)dt, \\
 dx_3(t) &= [AaS(x_1(t) - x_2(t)) - 2ax_3(t) - a^2x_0(t)]dt, \\
 dx_4(t) &= [Aa\{C_2S(C_1x_0(t)) + KS(y_2(t))\} - 2ax_4(t) - a^2x_1(t)]dt + Aadw(t), \\
 dx_5(t) &= [BbC_4S(C_3x_0(t)) - 2bx_5(t) - b^2x_2(t)]dt,
 \end{aligned} \tag{7}$$

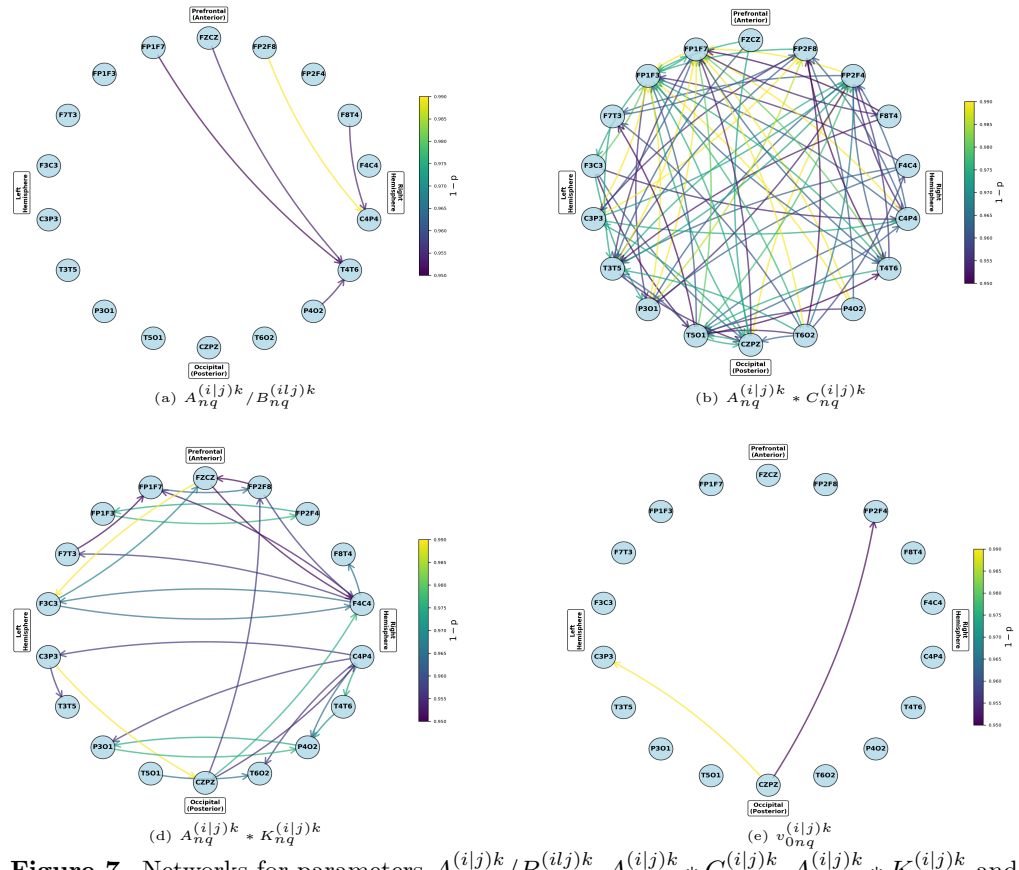


**Figure 7.** Networks for parameters  $A_{nq}^{(i|j)k} / B_{nq}^{(ilj)k}$ ,  $A_{nq}^{(i|j)k} * C_{nq}^{(i|j)k}$ ,  $A_{nq}^{(i|j)k} * K_{nq}^{(i|j)k}$  and  $v_{0nq}^{(i|j)k}$

with initial value  $\mathbf{x}_0 = (x_0(0), \dots, x_5(0))^T \in \mathbb{R}^6$  and the input  $y_2(t)$  from the external channel. We use the following Strang splitting method to generate the samples of  $\mathbf{x}(t)$  from the above model. See (Milstein and Tretyakov, 2003; Leimkuhler et al., 2016) for more details. To this end, we first divide the system (7) into two subsystems below:

$$\begin{aligned} dx_0^{[1]}(t) &= x_3^{[1]}(t)dt, \quad dx_1^{[1]}(t) = x_4^{[1]}(t)dt, \quad dx_2^{[1]}(t) = x_5^{[1]}(t)dt, \\ dx_3^{[1]}(t) &= [-2ax_3^{[1]}(t) - a^2x_0^{[1]}(t)]dt, \\ dx_4^{[1]}(t) &= \left[ -2ax_4^{[1]}(t) - a^2x_1^{[1]}(t) \right] dt, \\ dx_5^{[1]}(t) &= [-2bx_5^{[1]}(t) - b^2x_2^{[1]}(t)]dt, \end{aligned} \quad (8)$$

and

$$\begin{aligned} dx_0^{[2]}(t) &= 0, \quad dx_1^{[2]}(t) = 0, \quad dx_2^{[2]}(t) = 0, \\ dx_3^{[2]}(t) &= AaS\left(x_1^{[2]}(t) - x_2^{[2]}(t)\right)dt, \\ dx_4^{[2]}(t) &= Aa\left[C_2S\left(C_1x_0^{[2]}(t)\right) + KS(y_2(t))\right]dt + Aadw(t), \\ dx_5^{[2]}(t) &= BbC_4S\left(C_3x_0^{[2]}(t)\right)dt. \end{aligned} \quad (9)$$

Let  $\varphi_t^{[1]}$  and  $\varphi_t^{[2]}$  denote the exact flows of subsystems (8) and (9). Then, for  $\mathbf{x} \in \mathbb{R}^6$ , the so-called Strang splitting for system (7) can be written as

$$\psi_{\Delta t}(\mathbf{x}) = (\varphi_{\Delta t/2}^{[1]} \circ \varphi_{\Delta t}^{[2]} \circ \varphi_{\Delta t/2}^{[1]})(\mathbf{x}). \quad (10)$$

We independently generate the initial values for the states from the standard normal distribution. We choose the input signal  $y_2(t)$  from the channel F4C4 of the healthy subject H9 in the above EEG dataset which contains EEG measurements in the EEG channels for 18 pediatric subjects. Using the discretisation step size of  $h^{\text{sim}} = 1/256$ , we obtain the approximate solution paths for subsystems (8) and (9) over time-length  $T = 20$  seconds. We then calculate the output signal  $y_1(t) = x_1(t) - x_2(t)$ .

**Parameter sensitivity analysis.** In the following, taking the patient subject P3 as an example, given an time series from the channel C3P3, fitting ccDCM to the output time series from the chanel C4P4, we demonstrated that the excitation/inhibition ratio  $A/B$  was identifiable while the individual  $A$  and  $B$  were not.

To fit the NccDCM to the EEG data of subject P3, we calculated the loss functions and optimised them to find the estimates  $(\widehat{A}, \widehat{A/B}, \widehat{A*C}, \widehat{A*K}, \widehat{v}_0)$ . We plotted the loss functions in  $(\log A, A/B)$ , fixing  $A*C = \widehat{A*C}$ ,  $A*K = \widehat{A*K}$  and  $v_0 = \widehat{v}_0$ . The same procedure was also applied to the other pairs  $(\log A, A*C)$  and  $(\log A, A*K)$ . The results displayed in Fig. 8 indicated that all these loss functions were flat with respect to  $\log A$ , implying that  $A$  was not identifiable. Our finding was consistent with what was derived from the excitation/inhibition balance analysis for a canonical microcircuit model (Hauke et al., 2025). This also gave rise to a rationale for the reparameterisation of  $(A, B, C, K, v_0)$  by  $\theta = (A, A/B, A*C, A*K, v_0)$  in the Section 2.

**Bifurcation behavior of ccDCM.** Under the above simulation setting, we first demonstrate that the ccDCM does have bifurcation behavior when  $A/B$ ,  $C$ ,  $K$ , and  $v_0$  take values in some ranges. In the analysis, we change the value of one parameter with the fixed other parameters to their typical values as specified in Table 1. Figures 12(a) and 9 respectively display the input time series from the channel F4C4 of the healthy

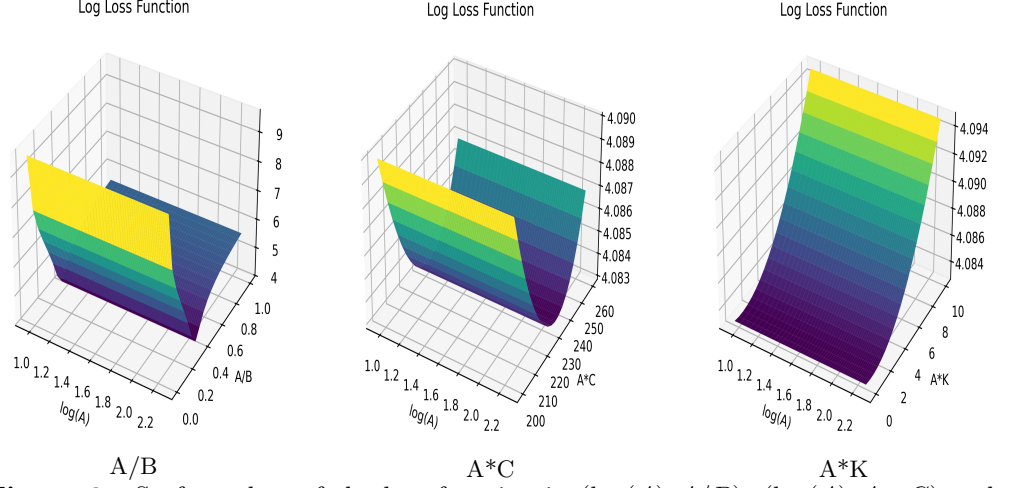


**Figure 8.** Surface plots of the loss function in  $(\log(A), A/B)$ ,  $(\log(A), A * C)$  and  $(\log(A), A * K)$ : The loss function is flat in  $\log(A)$ .

subject H9 and the corresponding output time series under varying values of  $A/B$ ,  $C$ ,  $K$ , and  $v_0$ .

As shown in Figure 9(a), the output signal remains stable for  $A/B = 2/25$  and  $3.25/22$ . However, when  $A/B$  increases to  $4/14$ , the output exhibits unstable oscillatory behavior after approximately 15 seconds. Note that, as depicted in Figure 12(a), the input signal reaches its maximum around this time. In the remaining panels of Figure 9, no similar phenomenon has been observed for the other parameters. Furthermore, the higher values of  $A/B$ ,  $K$ ,  $1/C$  and  $v_0$ , the higher output signals will result.

### 3.3.2 Absolute relative error of loss-based estimation

**Estimation of local nodes.** In the following, we assessed the absolute relative error of the proposed estimation for local nodes using a wide range of simulation studies.

In the simulations, EEG signals from the FP2F4, F4C4, C4P4, P4O2, FP1F3, F3C3, C3P3 and P3O1 channels were used as the input signal  $y_1(t)$ , obtained from one epileptic patient (P3) and healthy subject (H5). We repeatedly simulated  $y_1(t)$  from equations (7)  $M = 48$  times, giving 48 EEG segments of time series, each of a duration of 20 seconds. We set the simulation step size  $h^{\text{sim}} = 1/256$  and the epoch length of 2 to ensure that each epoch was short enough so that the Chen–Fliess series approximation was valid. We evaluate the proposed method with respect to the absolute relative error (ARE) for  $\widehat{\theta}_{2:5} = (\widehat{A/B}, \widehat{A * C}, \widehat{A * K}, \widehat{v}_0)$  for each of  $M$  EEG segments, where  $\text{ARE}(\widehat{\theta}_{2:5}) = |\widehat{\theta}_{2:5} - \theta_{2:5}^{(0)}|/|\theta_{2:5}^{(0)}|$  with  $\theta_{2:5}^{(0)}$  as the ground truth.

The parameters in the Equation (7) were set in the following three scenarios:

Scenario I.  $A = 3.25$ ,  $B = 22$ ,  $C = 135$ , and  $K = 50$  and  $v_0 = 6$ .

Scenario II.  $A = 4$ ,  $B = 14$ , and the remaining parameters are kept the same as in the Case I.

Scenario III.  $A \sim U(3, 6)$ ,  $B \sim U(17.6, 30)$ ,  $C \sim U(108, 160)$ ,  $K \sim U(0, 50)$  and  $v_0 \sim U(3.12, 9)$ , where  $U(a, b)$  is a uniform distribution over the interval  $[a, b]$ .

The simulation results, reported in Figures 10 and Table 2, showed that our proposed estimation is promising in terms of ARE.

**Joint estimation of nodes.** In the following, we assessed the absolute relative error of the proposed estimation for multiple nodes, where each node stands for a Jansen–Rit

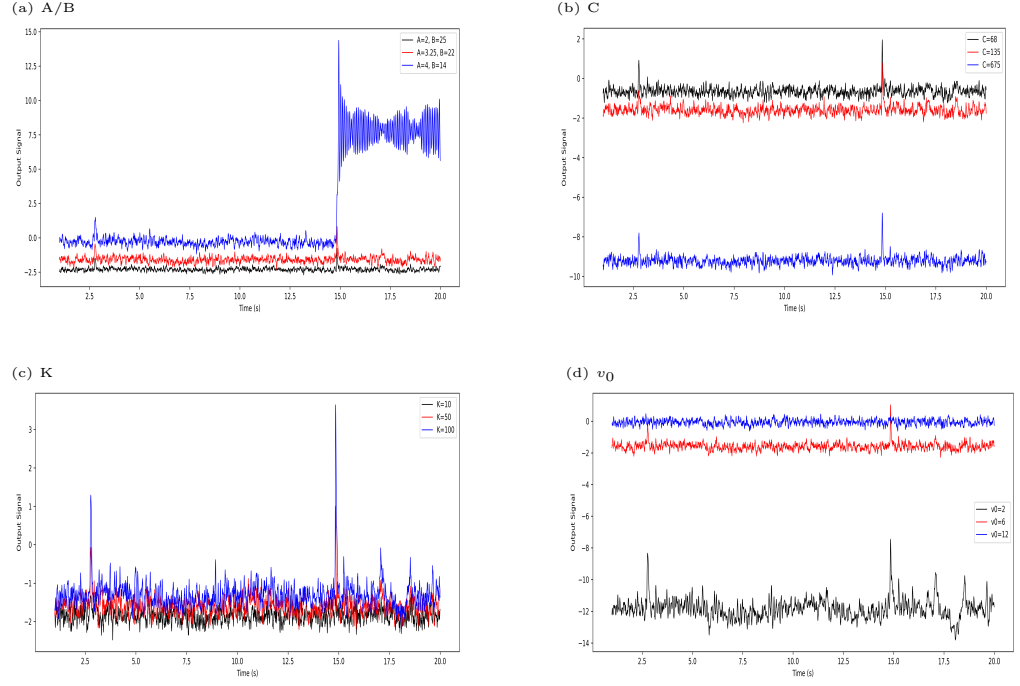


**Figure 9.** Given the input time series in Figure Output time-series for varying values of  $(A, B) \in \{(2, 15), (3.25, 22), (4, 14)\}$ ,  $C \in \{68, 135, 675\}$ ,  $K \in \{10, 50, 100\}$  and  $v_0 \in \{2, 6, 12\}$ . Output time-series exhibit bifurcation behavior only when  $A/B$  increases to 0.2857. The magnitude of output signal increases quickly in  $A/B$ ,  $v_0$  and  $1/C$  but slowly in  $K$ .

**Table 2.** The median of ARE for estimating ccDCM in (7). The left block for taking the EEG time series of the patient P3 as an input while the right block for taking the time series of healthy subject H5 as an input.

Parameter	P3			Parameter	H5		
	Scenario I	Scenario II	Scenario III		Scenario I	Scenario II	Scenario III
$A/B$	0.09	0.10	0.09	$A/B$	0.10	0.09	0.09
$A * C$	0.05	0.02	0.05	$A * C$	0.05	0.03	0.05
$v_0$	0.06	0.08	0.06	$v_0$	0.06	0.07	0.07
$A * K$	0.08	0.10	0.10	$A * K$	0.11	0.14	0.10
$A$	0.25	0.25	0.25	$A$	0.44	0.25	0.29

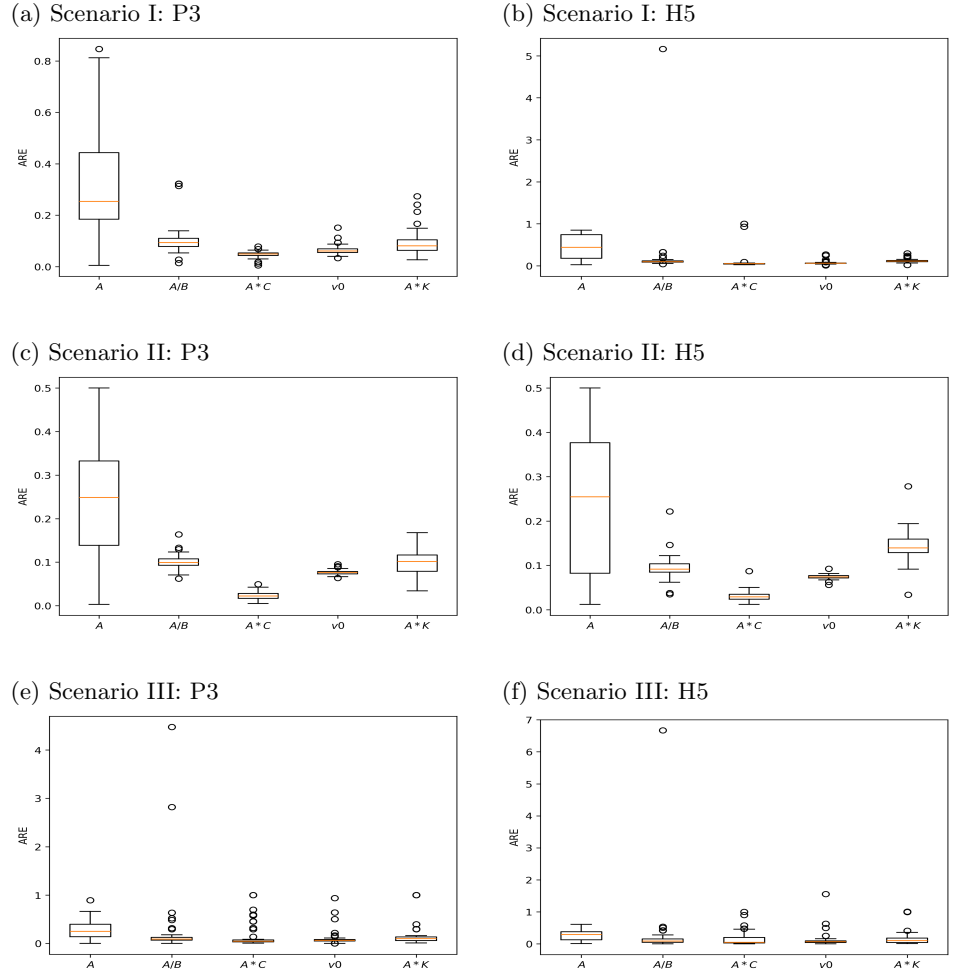


**Figure 10.** Box-plots of ARE values of the estimated  $A$ ,  $A/B$ ,  $A*C$ ,  $v_0$  and  $A*K$  compared to the ground truths for scenarios I to III.

---

neural mass model. The multiple nodes were coupled in a unidirectional ring structure, allowing one node to influence another node. For each node, the corresponding parameters were estimated independently using the proposed estimation method. The simulation was repeated  $M = 100$  times. The morel details of the setting for the case of three nodes system can be found in the Appendix Sf, the Supplementary Material. The corresponding ARE values, summarized in Figure 4 and Table 6 in the Appendix Sf, the Supplementary Material, showed a good accuracy of the estimation. However, our simulation experience (not shown here) indicated that the performance would be deteriorated when there were multiple external inputs of similar magnitudes to a node.

## 4 Discussion and conclusions

**Enabling data-driven composite network modelling at whole brain scales.** The question as to how large-scale dynamic causal patterns emerge from underlying neuronal interactions is one that has attracted much interest in neurological disease studies (Friston et al., 2019; Forrester et al., 2020; Pereira et al., 2021; Forrester et al., 2024; Singh et al., 2025) and in statistics (Pokern et al., 2009; Ditlevsen et al., 2025). The existing imaging studies often focused on a single subject study, either with models for a small number of cortical columns or with models in a large scale but involving only excitatory/inhibitory neuron populations or with models in a large scale but for homogeneous brain regions, where all nodes in the network models are identical. In this paper, to relax the above limitations, we have proposed a heterogeneous composite network model, NccDCM, for groups of EEG scans respectively. In the NccDCM, each node represents a local Jansen-Rit neural mass model for describing synaptic interactions in excitatory/inhibitory and pyramidal neuron populations, which consists of six-dimensional stochastic differential equations, while directed edges stand for coupling/transmissions between these local neuron populations across different channels. To account for individual subject-variability, we have introduced a mixed-effects model for network parameters. We have developed the Chen-Fliess expansion-based evolutionary optimisation algorithm for estimating NccDCMs. For easy of exposition, we have adopted a pairwise screening strategy to estimate edges in the proposed composite network. To identify dynamic causal nets that differs cases from controls, we have carried out a post-analysis of variance for estimated parameters in cases and controls. The work-flow is displayed in Figure 12. In the simulation study presented here, we have revealed that the excitation and inhibition parameters are not well-identifiable although their ratio is identifiable. A similar phenomenon has been found in conductance-based DCM by Hauke et al. (2025). This has given rise to the approach of re-parametrisation of the original parameters that the new parameters, including the excitation/inhibition balance ratio, are identifiable except the excitation parameter. We have assessed the absolute relative errors of the model estimation, demonstrating that the performance of the proposed estimates for the node and edge parameters is relatively accurate.

**Detecting and qualifying differential epileptic network.** Epilepsy is considered a network disease that affects the brain across multiple levels of spatial and temporal scales. The epileptic network, however, is not static but evolves in time which requires novel approaches for an in-depth characterization (Bröhl et al., 2024). The proposed biophysics-informed network of neural mass models aims to detect and quantify such a network. In particular, we have pursued a computational approach to elucidating the difference of brain dynamic connectivity patterns called dynamic causal nets between cases and controls or between the preictal period and the ictal period. We first fitted a NccDCM to the EEG scan for each subject in the case and control groups respectively.

---

---

Following that, a mixed-effects model-based post-analysis of variance has been conducted to contrast estimated case-control parameters. This has given rise to various differential causal nets that differ the case-networks from the control-networks. The same analysis has also been performed on the segments of time series in preictal and ictal periods. We have found similar differential causal nets that differ the preictal period from the ictal period. These nets are associated with epileptic seizures even after the Benjamini-Hochberg correction for multiple testing.

It is widely recognised that EEG scans are inherently noisy with weak signals due to the minuscule amplitude of brain-generated electrical activity recorded at the scalp and the susceptibility to various sources of contamination. Only the synchronous firing of millions of neurons produces a measurable signal at the scalp. Despite this, we have demonstrated the advantage of the NccDCM analysis over the conventional temporal correlation-based analysis in detecting links between regions. We have identified a list of dynamic causal nets to characterise the spatial-temporal varying epileptic network. These differential dynamic causal nets partially covered default mode network (DMN), a collection of distributed and interconnected brain regions. DMN is typically suppressed when the brain receives external stimuli; however, in the absence of attention to external stimuli, the DMN switches to internally focused thought processes. Therefore, the DMN activity can be observed in subject's resting states. It follows from Menon (2023) that the DMN nodes include posterior cingulate cortex (PCC) and retrosplenial cortex (RSC) in posterior medial parietal cortex; medial prefrontal cortex PFC (mPFC) with its dorsomedial (dmPFC) and ventromedial (dmPFC) subdivisions; anterior temporal cortex (ATC); middle temporal gyrus (MTG) in lateral temporal cortex; medial temporal lobe (MTL); and angular gyrus (AG) in lateral parietal cortex; thalamus (THAL) and caudate nucleus (CAU). Activities in PCC and RSC are captured by electrodes FP2, P3, P4 and O2; AG is captured by P3, P4, T5 and T6; PFC is captured by FP1, FP2, Fz, F3 and F4; ATC is captured by T3 and T4; MTG is captured by T5 and T6; MTL is captured by F3, T4, T5, and T6. EEG channels do not directly cover subcortical structures like the thalamus (THAL) and caudate nucleus (CAU) because these deep brain regions do not produce sufficient electrical signals that reach the scalp surface to be localised to a single channel. In Figures 4 and 5, the identified dynamic causal nets differ cases from controls in the means and variations of the estimated NccDCM parameters. These nets imply epilepsy-predisposed changes in the DMNs and the THAL: (a) Edge changes in the excitatory/inhibitory synaptic ratio: AG/PCC points to PFC, THAL points to AG/PCC. (b) Many edge changes in the local structure parameters  $A * C$ . (c) Changes in the transmission parameter  $A * K$ : ATC points to PFC; AG points to PFC. (d) Edge changes in  $v_0$ : AG points to PFC; ATC points to PFC. Figures 7, compared the ictal period to the preictal period, yields many dynamic causal nets that have been related to the estimated region-transmission parameters. This finding implies that the changes in the region-transmission parameters can be used for predicting onset of seizures.

Our findings have provided a few epileptic network configurations than the DMN, highlighting the contribution of dysfunctions in the DMN to epileptic activities and cognitive behaviors in patients e.g., ( e.g., Jiang et al., 2022). As seizures are caused by abnormal over-firing of the brain, it is expected that the excitation/inhibition ratio/local connectivity/region connectivity-driven hyperactivity in the patients' DMN and thalamus/caudate nucleus should be associated with epilepsy.

**Limitations.** We view our present model as having the following limitations: 1) algorithms for estimating the NccDCM and 2) the omission of subjects' demographic information. We have developed a marginal screening approach to estimating the channel-wise connection parameters. Marginal screening is a method used to estimate

---

the coefficients of multiple external channel inputs by identifying the most significant coefficients for each channel. This approach is particularly useful when a large number of nodes involved. The method involves constructing a model that includes all external channels and then selecting the most significant channels to include in the final model. This method helps to avoid overfitting and ensures that the model is generalisable to new data. However, the method is at the cost of estimation efficiency. The penalisation regression or forward/backward variable selection can be explored in the future. The second limitation potentially arise from the neglect of subjects' demographic information such as age and gender. A further work is needed to take age and gender as additional predictors in each ccDCM.

**Conclusions and future work.** In summary, the proposed NccDCM is a novel and useful tool for detecting disease-predisposed effective connectivity in case-control study using EEG data. We have shown that the NccDCM can be used to characterise epileptic brain network at the whole brain scale. This work can be extended to the source-level, in particular, those sources in the deep brain, and to other neural mass models in Friston et al. (2019).

## Appendix A

Consider the following set of differential system of the form

$$\dot{z}(t) = g_0(z(t)) + \sum_{i=1}^m g_i(z(t))u_i(t), \quad z(0) = z_0; \quad y(t) = h(z(t)), \quad (11)$$

where each  $g_i$  is an analytic vector field expressed in some neighborhood of  $z_0$ , and the  $h$  is an analytic output function. Assume that (11) has a well defined solution  $z(t)$ ,  $t \in [t_0, T + t_0]$  for any given input  $u_i(t)$ , and  $y(t) = h(z(t))$ ,  $t \in [t_0, T + t_0]$ .

**Lemma** . The solution to equation (11) can be expressed as a Chen-Fliess series of the form

$$\begin{aligned} y(t) = & \sum_{1 \leq i_1, \dots, i_k \leq m, k \geq 0} \left( \int_0^t \int_0^{\tau_k} \dots \int_0^{\tau_2} u_{i_k}(\tau_k) \dots u_{i_1}(\tau_1) d\tau_1 \dots d\tau_{k-1} d\tau_k \right) \\ & \times \left( L_{g_{i_1}} \circ \dots \circ L_{g_{i_k}} h(z_0) \right), \end{aligned} \quad (12)$$

where  $L_{g_{i_1}} \circ \dots \circ L_{g_{i_k}} h(z_0)$  is a Lie-derivative in the direction of the vector field. See Lyons (1998).

**Chen-Fliess expansion of states in model (7)).** For a small increment  $h$  and  $t \in [t_0, t_0 + h]$ , truncating the Chen-Fliess expansion of  $x_0(t)$  and  $x_2(t)$  at the 3rd order, we have

$$\begin{aligned} x_0(t) = & x_0(t_0) + x_3(t_0)(t - t_0) + \left( \frac{\nu_{\max} A a}{1 + e^{r(v_0 - y(t_0))}} - a^2 x_0(t_0) - 2a x_3(t_0) \right) \frac{(t - t_0)^2}{2} \\ & + \left( \frac{r \nu_{\max} A a e^{r(v_0 - y(t_0))} \dot{y}(t_0)}{(1 + e^{r(v_0 - y(t_0))})^2} - a^2 x_3(t_0) \right. \\ & \left. - 2a \left( \frac{\nu_{\max} A a}{1 + e^{r(v_0 - y(t_0))}} - a^2 x_0(t_0) - 2a x_3(t_0) \right) \right) \frac{(t - t_0)^3}{3!} + O_p((t - t_0)^4) \end{aligned} \quad (13)$$

$$\begin{aligned}
x_2(t) = & x_2(t_0) + x_5(t_0)(t - t_0) + \left( \frac{\nu_{\max} BbC_4}{1 + e^{r(v_0 - C_{31}x_0(t_0))}} - 2bx_5(t_0) - b^2x_2(t_0) \right) \frac{(t - t_0)^2}{2} \\
& + \left( \frac{r\nu_{\max} BbC_3C_4x_3(t_0)e^{r(v_0 - C_{31}x_0(t_0))}}{(1 + e^{r(v_0 - C_{31}x_0(t_0))})^2} - b^2x_5(t_0) \right. \\
& \left. - 2b \left( \frac{\nu_{\max} BbC_4}{1 + e^{r(v_0 - C_{31}x_0(t_0))}} - 2bx_5(t_0) - b^2x_2(t_0) \right) \right) \frac{(t - t_0)^3}{3!} + O_p((t - t_0)^4) \quad (14)
\end{aligned}$$

Similarly, given the input  $y^{(j)}(t)$  from channel  $j$ , truncating the Chen-Fliess expansion of  $x(t)$  at the 2nd order, we have

$$\begin{aligned}
x_1(t) = & x_1(t_0) + x_4(t_0)(t - t_0) \\
& + \left( \frac{\nu_{\max} AaC_2}{1 + e^{r(v_0 - C_1x_0(t_0))}} + \frac{\nu_{\max} AaK}{1 + e^{r(v_0 - y^{(j)}(t_0))}} - a^2x_1(t_0) - 2ax_4(t_0) \right) \frac{(t - t_0)^2}{2} \\
& + Aa \int_{t_0}^t (t - s) d\tilde{w}_s + o_p((t - t_0)^3), \quad (15)
\end{aligned}$$

It follows from equations (14) and (15) that the truncated Chen-Fliess expansion of  $y(t)$  at the 2nd order can be written as

$$y(t) \approx g(t|x_{-\{3\}}(t_0), y(t_0), \dot{y}(t_0), y^{(j)}(t_0), \boldsymbol{\theta} + Aa \int_{t_0}^t (t - s) d\tilde{w}_s, \quad (16)$$

where

$$\begin{aligned}
g(t|x_{-\{3\}}(t_0), y(t_0), \dot{y}(t_0), y^{(j)}(t_0), \boldsymbol{\theta}) = & y(t_0) + \dot{y}(t_0)(t - t_0) \\
& + \left( \frac{\nu_{\max} AaC_2}{1 + e^{r(v_0 - C_1x_0(t_0))}} + \frac{\nu_{\max} AaK}{1 + e^{r(v_0 - y^{(j)}(t_0))}} - a^2x_1(t_0) - 2ax_4(t_0) \right) \frac{(t - t_0)^2}{2} \\
& - \left( \frac{\nu_{\max} BbC_4}{1 + e^{r(v_0 - C_{31}x_0(t_0))}} - 2bx_5(t_0) - b^2x_2(t_0) \right) \frac{(t - t_0)^2}{2}.
\end{aligned}$$

It is clear that  $g$  function depends on the initial values of states  $x_{-\{3\}}(t_0)$ .

Let

$$\begin{aligned}
L_A(t_0) &= \left( \frac{\nu_{\max} Aa}{1 + e^{r(v_0 - y(t_0))}} - a^2x_0(t_0) - 2ax_3(t_0) \right) \\
L_B(t_0) &= \left( \frac{\nu_{\max} BbC_4}{1 + e^{r(v_0 - C_{31}x_0(t_0))}} - 2bx_5(t_0) - b^2x_2(t_0) \right).
\end{aligned}$$

The 3rd-order Chen-Fliess series of  $x_0$  and  $x_2$  are

$$\begin{aligned}
g_0(t|x_{0,3}(t_0), y(t_0), \dot{y}(t_0)) = & x_0(t_0) + x_3(t_0)(t - t_0) + L_A(t_0) \frac{(t - t_0)^2}{2} \\
& + \left( \frac{r\nu_{\max} Aae^{r(v_0 - y(t_0))}\dot{y}(t_0)}{(1 + e^{r(v_0 - y(t_0))})^2} - a^2x_3(t_0) - 2aL_A(t_0) \right) \frac{(t - t_0)^3}{3!}, \quad (17)
\end{aligned}$$

and

$$\begin{aligned}
g_2(t|x_{-\{1,4\}}(t_0)) = & x_2(t_0) + x_5(t_0)(t - t_0) + L_B(t_0) \frac{(t - t_0)^2}{2} \\
& + \left( \frac{r\nu_{\max} BbC_3C_4x_3(t_0)e^{r(v_0 - C_{31}x_0(t_0))}}{(1 + e^{r(v_0 - C_{31}x_0(t_0))})^2} - b^2x_5(t_0) - 2bL_B(t_0) \right) \\
& \times \frac{(t - t_0)^3}{3!}, \quad (18)
\end{aligned}$$

respectively.

The 2nd-order Chen-Fliess series of  $x_3$  and  $x_5$  are

$$\begin{aligned} g_3(t|x_{\{0,3\}}(t_0), y(t_0), \dot{y}(t_0)) &= x_3(t_0) + L_A(t_0)(t - t_0) \\ &+ \left( \frac{r\nu_{\max} A a e^{r(v_0 - y(t_0))} \dot{y}(t_0)}{(1 + e^{r(v_0 - y(t_0))})^2} - a^2 x_3(t_0) - 2a L_A(t_0) \right) \\ &\times \frac{(t - t_0)^2}{2}, \end{aligned} \quad (19)$$

and

$$\begin{aligned} g_5(t|x_{\{1,4\}}(t_0)) &= x_5(t_0) + L_B(t_0)(t - t_0) \\ &+ \left( \frac{r\nu_{\max} B b C_3 C_4 x_3(t_0) e^{r(v_0 - C_3 x_0(t_0))}}{(1 + e^{r(v_0 - C_3 x_0(t_0))})^2} - b^2 x_5(t_0) - 2b L_B(t_0) \right) \\ &\times \frac{(t - t_0)^2}{2}, \end{aligned} \quad (20)$$

respectively.

## Author Contributions

K.Y. conceptualisation, methodology, coding, data analysis, writing & editing of original draft; G.G. conceptualisation, methodology, review & editing of original draft; J.Z. conceptualisation, methodology, coding, data analysis, writing and editing of original draft, supervision, funding acquisition and project administration.

## Data and Code Availability

Codes to reproduce simulation results are in <https://github.com/zhangjsib/NccDCM>. The EEG data on epilepsy is publicly available in OK et al. (2021).

## Funding

The research of K.Y. and J.Z. is supported by the Engineering and Physical Sciences Research Council (EPSRC) grant (EP/X038297/1)..

## Declaration of Competing Interests

K.Y. and J.Z. have no competing interests. G.G. is an employee of Innovision IP Ltd which provides commercial reports on individuals who may have had a head injury.

## Acknowledgments

We are grateful to the University of Kent for letting us use the University HPC service.

---

## Supplementary material

Supplementary material in a pdf file includes additional information as follows.

Appendix Sa: An introduction on the optimisation algorithm JADE.

Appendix Sb: Lagged temporal correlation-based functional connectivity.

Appendix Sc: EEG electrode allocation on the scalp.

Appendix Sd: Post-ANOVA tables.

Appendix Se: More results on subject-heterogeneity analysis.

Appendix Sf: A simulation study on the estimation of three-nodes NccDCMs.

The pdf file of the Supplementary Material is available in  
<https://github.com/zhangjsib/NccDCM>.

Differential Dynamic Causal Nets: Model Construction,  
Identification and Group Comparisons

—Supplementary Material

## Supporting information

In this supplementary material, we will present (a) the optimisation algorithm JADE; (b) the lagged correlation-based functional connectivity; (c) the standard allocation of the electrodes on the scalp; (d) post-ANOVA tables; (e) more results on subject-heterogeneity analysis; (f) simulation study on the three-nodes system.

## Appendix Sa: The optimisation algorithm JADE

To minimize the forward loss function, we employed a novel adaptive differential evolution with optional external archive (JADE), a population-based global optimization method proposed by Zhang and Sanderson (2009) and implemented in the `mealpy` library. JADE is well suited for non-convex, multi-modal, and non-differentiable optimization problems, as it does not rely on gradient information. Instead, it evolves a population of candidate solutions through mutation, crossover, and selection, with the aim of converging to the global minimum. The method is particularly advantageous in our context because the objective function may be non-smooth or contain multiple local minima due to the models nonlinear structure.

As a metaheuristic optimization algorithm, the performance of JADE is sensitive to the choice of hyperparameters, the initial population size and epoch size. These two hyperparameters substantially affect both the convergence speed and the quality of the final solution.

Figure 11 illustrates how the value of the loss function evolves under different settings of population size and iteration number in simulation studies, emphasizing the role of these hyperparameters in shaping optimisation performance. It is evident that almost algorithm JADE eventually converges to the same optimal value when the number of iterations exceeds 150 for almost all population sizes. Intuitively, smaller populations may force the algorithm to converge to a local minimum, limiting the coverage of its search space. In contrast, larger populations generally facilitate faster convergence owing to enhanced diversity, though further increases in population size yield diminishing returns in performance while incurring substantially higher computational costs. To strike a balance between convergence accuracy and computational efficiency, we set the population size and the maximum number of iterations to 15 and 250, respectively.

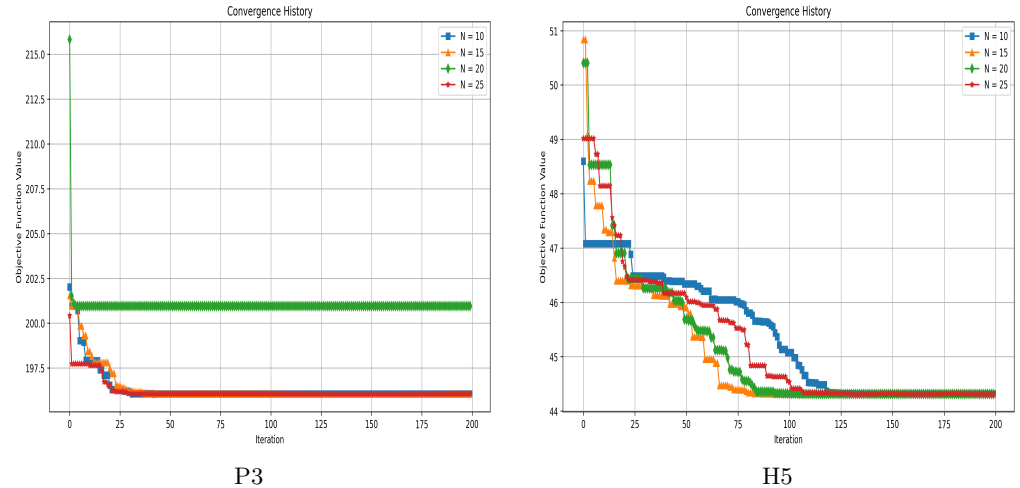


**Figure 11.** Trace plots of the objective function/loss function as the number of iterations is increasing: L-SHAPE under different population sizes.

## Appendix Sb: Lagged correlation-based functional connectivity

We calculate the functional connectivity based on the lagged correlation coefficient. The EEG signals used are extracted from the same time block across all subjects and from

all channels. For each subject, we compute pairwise cross-correlations between all channel pairs across time lags ranging from  $-50$  to  $+50$ . For each channel pair, the maximum absolute correlation across these time lags is calculated, which allows us to construct correlation matrices for all subjects.

To normalise the correlation values, we apply Fisher's  $z$ -transform, yielding the matrices  $F_{P_i}$  ( $1 \leq i \leq n_0$ ) and  $F_{H_j}$  ( $1 \leq j \leq n_1$ ). For the control and case groups, the mean matrices are then computed as  $\bar{F}_P = \frac{1}{n_0} \sum_{i=1}^{n_0} F_{P_i}$ ,  $\bar{F}_H = \frac{1}{n_1} \sum_{j=1}^{n_1} F_{H_j}$ . Then, the corresponding variance matrices are defined as  $\bar{V}_P = \frac{1}{n_0} \sum_{i=1}^{n_0} (F_{P_i} - \bar{F}_P)^2$  and  $\bar{V}_H = \frac{1}{n_1} \sum_{j=1}^{n_1} (F_{H_j} - \bar{F}_H)^2$ . Let  $\bar{\rho}_{ij}^{(0)}$ ,  $\bar{\rho}_{ij}^{(1)}$ ,  $\bar{\varrho}_{ij}^{(0)}$ , and  $\bar{\varrho}_{ij}^{(1)}$  denote the  $(i, j)$ -th elements of  $\bar{F}_P$ ,  $\bar{F}_H$ ,  $\bar{V}_P$ , and  $\bar{V}_H$ , respectively. For each channel pair, we compute the  $z$ -score as

$$f_{ij} = \frac{\bar{\rho}_{ij}^{(0)} - \bar{\rho}_{ij}^{(1)}}{\sqrt{\frac{(n_0 - 1) \bar{\varrho}_{ij}^{(0)} + (n_1 - 1) \bar{\varrho}_{ij}^{(1)}}{n_0 + n_1 - 2}}}.$$

Finally, only the values of  $|f_{ij}|$  greater than 0.5 are retained, and the results are based on the absolute  $z$ -scores.

In addition, we apply the following permutation test procedure to compute the  $p$ -values.

1. **Permutation procedure.** Let  $\mathcal{D} = (H_1, \dots, H_{10}, P_1, P_3, P_5, \dots, P_{10})$  denote the combined dataset. To assess the statistical significance of the observed  $F = (f_{ij})$ , we apply a permutation test: the labels "case" and "control" are randomly reassigned by permuting  $\mathcal{D}$ . In each permutation, the first 10 subjects in the permuted dataset  $\mathcal{D}^\pi$  are designated as the control group and the remaining subjects as the case group. Then, we recompute the test statistic  $f_{ij}^\pi$ .
2. **Significance assessment.** This permutation procedure is repeated 999 times. The observed statistic  $f_{ij}$  is included as part of the permutation distribution  $\{f_{ij}^\pi\}$ . The empirical  $p$ -value is then given by

$$p = \frac{\#\{|f_{ij}^\pi| \geq |f_{ij}|\}}{\text{Total number of permutations}},$$

where the numerator counts the number of permuted statistics at least as extreme as the observed  $f_{ij}$ .

## Appendix Sc: EEG electrode allocation on the scalp

Figures 12 and 3 show the positions of the electrodes and the brain regions that the channels belong to.

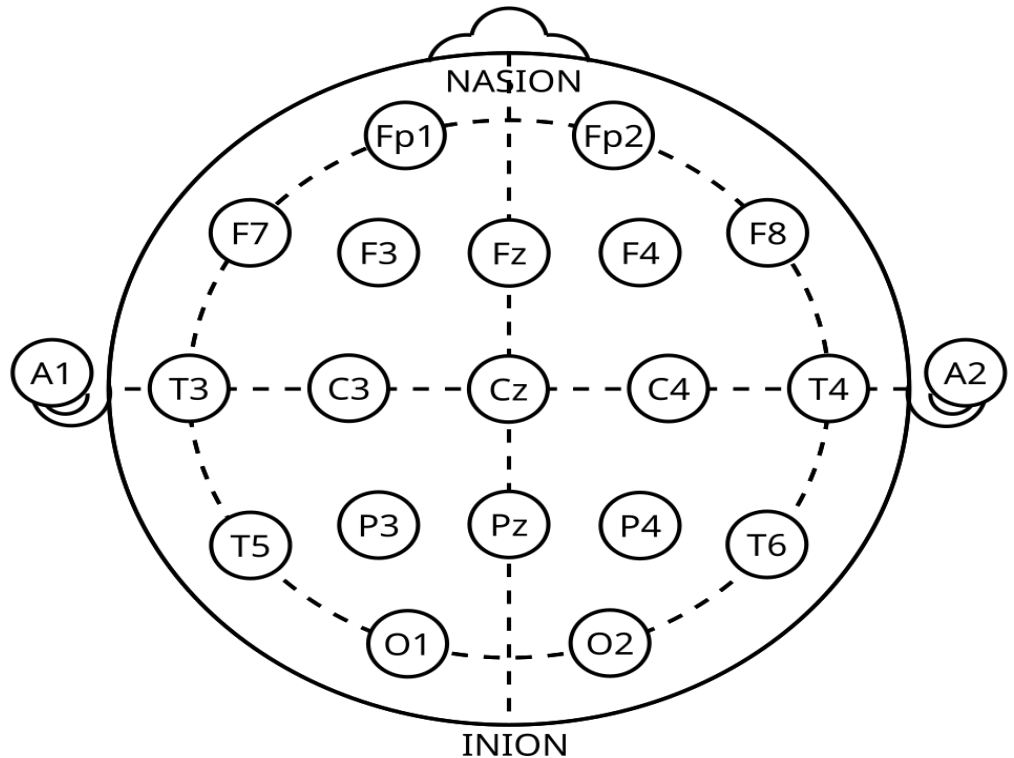


**Figure 12.** The International 10-20 System for EEG Electrode Placement which was adopted from <https://en.wikipedia.org/wiki>.

**Table 3.** EEG electrode pairs and their brain regions

Electrode pair	Position	Brain Region
FP2F4	Right frontopolar	Right prefrontal cortex
P4O2	Right parieto-occipital	Visual association
F4C4	Right fronto-central	Right frontal → motor cortex
F3C3	Left fronto-central	Left frontal → motor cortex
C4P4	Right centro-parietal	Right sensorimotor → parietal
C3P3	Left centro-parietal	Left sensorimotor → parietal
FP1F3	Left frontopolar	Left prefrontal cortex
P3O1	Left parieto to occipital	Visual cortex
FP2F8	Right frontopolar	Anterior inferior frontal
F8T4	Right inferior frontal	Broca homolog
T4T6	Right mid to posterior temporal	Auditory association
T6O2	Right posterior temporal	Visual association
FP1F7	Left frontopolar	Anterior inferior frontal cortex
F7T3	Left inferior frontal	Broca area vicinity
T3T5	Left mid to posterior temporal lobe	Auditory and language
T5O1	Left posterior temporal to occipital	Visual association
FZCZ	Medial frontal cortex	Supplementary motor
CZPZ	Central midline to parietal midline	Primary motor
BP3REF	A reference electrode	Not a cortical region

## Appendix Sd: Post-ANOVA tables

The results of the post ANOVA are summarised in Tables 4-7. The results indicated that the identified dynamic causal nets were highly significant for each parameter.

**Table 4.** Post ANOVA:  $A_{nq}^{(i|j)k} / B_{nq}^{(ilj)k}$ .

Factor	Df	Sum of Sq.	R <sup>2</sup>	F	p-value
Case-control	1	113.082	0.0167	93.150	0.0002
Channels	305	404.262	0.0596	1.092	0.0350
Case-control $\times$ Channels	305	324.793	0.0479	0.877	0.9950
Residual	4896	5943.652	0.8759	—	—
Total	5507	6785.790	1.0000	—	—

**Table 5.** Post ANOVA table for  $A_{nq}^{(i|j)k} * C_{nq}^{(i|j)k}$ .

Factor	Df	Sum of Sq.	R <sup>2</sup>	F	p-value
Case-control	1	$1.478 \times 10^9$	0.114	715.823	0.0002
Channels	305	$6.871 \times 10^8$	0.053	1.091	0.0916
Case-control $\times$ Channels	305	$6.539 \times 10^8$	0.051	1.038	0.2796
Residual	4896	$1.011 \times 10^{10}$	0.782	—	—
Total	5507	$1.293 \times 10^{10}$	1.000	—	—

**Table 6.** Post ANOVA table for  $A_{nq}^{(i|j)k} * K_{nq}^{(i|j)k}$

Factor	Df	Sum of Sq.	R <sup>2</sup>	F	p-value
Case-control	1	$3.161 \times 10^8$	0.074	580.963	0.0002
Channels	305	$9.121 \times 10^8$	0.213	5.496	0.0002
Case-control $\times$ Channels	305	$3.957 \times 10^8$	0.092	2.384	0.0002
Residual	4896	$2.664 \times 10^9$	0.621	—	—
Total	5507	$4.288 \times 10^9$	1.000	—	—

## Appendix Se: More results on subject-heterogeneity analysis

We present results of subject-heterogeneity analysis for FP1F7, C4P4, T6O2, T5O1 and P4O2.

## Appendix Sf: A simulation study on the estimation of three-nodes NccDCMs

In this appendix, we conducted a simulation study based on the NccDCM of three nodes, where each node was represented by a Jansen–Rit neural mass model. The three nodes were coupled in a unidirectional ring structure. The resulting three-node

**Table 7.** Post multivariate ANOVA table for  $v_{0nq}^{(i|j)k}$

Factor	Df	Sum of Sq.	R <sup>2</sup>	F	p-value
Case-control	1	$3.639 \times 10^5$	0.184	1255.748	0.0002
Channels	305	$1.226 \times 10^5$	0.062	1.387	0.0002
Case-control $\times$ Channels	305	$6.896 \times 10^4$	0.035	0.780	0.9998
Residual	4896	$1.419 \times 10^6$	0.719	—	—
Total	5507	$1.974 \times 10^6$	1.000	—	—

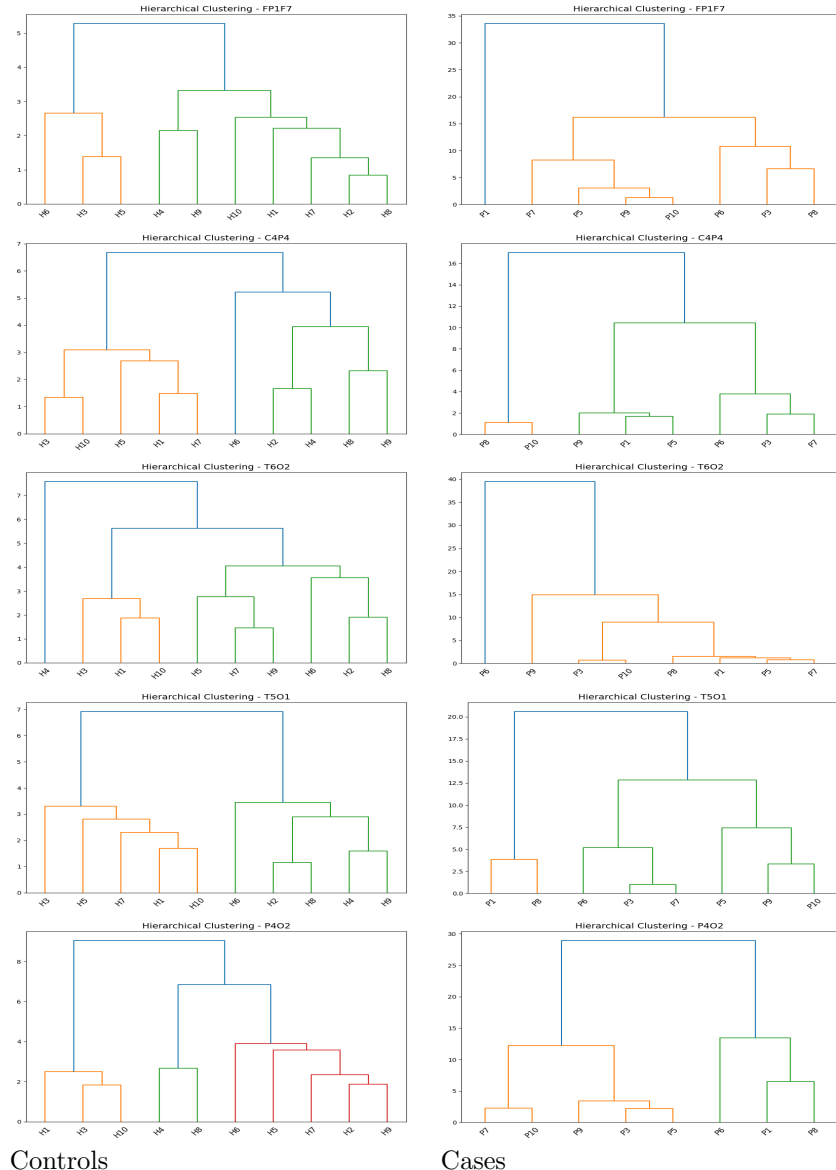


**Figure 13.** Dendrograms for the channels FP1F7, C4P4, T6O2, T5O1 and P4O2. The left panel is for the control group (the left panel) while the right panel is for the case group.

dynamical system was described by the following 18 stochastic differential equations:

$$\begin{aligned}
dx_0(t) &= x_3(t)dt, \quad dx_1(t) = x_4(t)dt, \quad dx_2(t) = x_5(t)dt, \\
dx_3(t) &= [A_1 a S_1 (x_1(t) - x_2(t)) - 2ax_3(t) - a^2 x_0(t)] dt, \\
dx_4(t) &= [A_1 a \{C_{21} S_1 (C_{11} x_0(t)) + K_1 S_1 (x_{13}(t) - x_{14}(t))\} \\
&\quad - 2ax_4(t) - a^2 x_1(t)] dt + A_1 a dw(t), \\
dx_5(t) &= [B_1 b C_{41} S_1 (C_{31} x_0(t)) - 2bx_5(t) - b^2 x_2(t)] dt, \\
dx_6(t) &= x_9(t)dt, \quad dx_7(t) = x_{10}(t)dt, \quad dx_8(t) = x_{11}(t)dt, \\
dx_9(t) &= [A_2 a S_2 (x_7(t) - x_8(t)) - 2ax_9(t) - a^2 x_6(t)] dt, \\
dx_{10}(t) &= [A_2 a \{C_{22} S_2 (C_{12} x_6(t)) + K_2 S_2 (x_1(t) - x_2(t))\} \\
&\quad - 2ax_{10}(t) - a^2 x_7(t)] dt + A_2 a dw(t), \\
dx_{11}(t) &= [B_2 b C_{42} S_2 (C_{32} x_6(t)) - 2bx_{11}(t) - b^2 x_8(t)] dt, \\
dx_{12}(t) &= x_{15}(t)dt, \quad dx_{13}(t) = x_{16}(t)dt, \quad dx_{14}(t) = x_{17}(t)dt, \\
dx_{15}(t) &= [A_3 a S_3 (x_{13}(t) - x_{14}(t)) - 2ax_{15}(t) - a^2 x_{12}(t)] dt, \\
dx_{16}(t) &= [A_3 a \{C_{23} S_3 (C_{13} x_{12}(t)) + K_3 S_3 (x_7(t) - x_8(t))\} \\
&\quad - 2ax_{16}(t) - a^2 x_{13}(t)] dt + A_3 a dw(t), \\
dx_{17}(t) &= [B_3 b C_{43} S_3 (C_{33} x_{12}(t)) - 2bx_{17}(t) - b^2 x_{14}(t)] dt,
\end{aligned} \tag{21}$$

with the initial condition  $\mathbf{x}_0 = (x_0(0), \dots, x_{17}(0))^\top \in \mathbb{R}^{18}$  and

$$S_i(x(t)) = \frac{\nu_{\max}}{1 + \exp(r(\nu_{0i} - x(t)))}, \quad t \in [0, T], \quad i = 1, 2, 3.$$

The first three, the second three and the last three equations were corresponding to nodes I, II and III respectively. For nodes I, II and III, we defined the observed outputs as  $y_1(t) = x_1(t) - x_2(t)$ ,  $y_2(t) = x_7(t) - x_8(t)$ , and  $y_3(t) = x_{13}(t) - x_{14}(t)$ . Let  $\mathbf{Y}(t) = (y_1(t), y_2(t), y_3(t))^\top$  denote the multi-node output process.

The inter-channel coupling structure was specified as follows: the input to node I is  $y_3(t)$ , the input to node II is  $y_1(t)$ , and the input to node III is  $y_2(t)$ . Consequently, the three-node system formed a directed cyclic network  $y_3(t) \rightarrow y_1(t) \rightarrow y_2(t) \rightarrow y_3(t)$ .

As before, we employed the Strang splitting method to generate sample paths of  $\mathbf{Y}(t)$  from the coupled system (21). We independently generated the initial values of the states from the standard normal distribution.

The underlying values parameters in equation (21) were set as follows:  $A_1 = 3.25$ ,  $B_1 = 22$ ,  $C_1 = 135$ ,  $K_1 = 50$ ,  $\nu_{01} = 6$ ;  $A_2 = 4$ ,  $B_2 = 14$ ,  $C_2 = 135$ ,  $K_2 = 70$ ,  $\nu_{02} = 4$ ;  $A_3 = 3$ ,  $B_3 = 15$ ,  $C_3 = 135$ ,  $K_3 = 50$ , and  $\nu_{03} = 5$ .

For each channel, the corresponding parameters were estimated independently using the proposed estimation method. The simulation was repeated  $M = 100$  times. The resulting corresp ARE values were summarized in Figure 14 and Table 8.

As shown in Figure 14 and Table 8, the proposed method demonstrated a good performance in the case where nodes are dynamically coupled each other.

## References

Ableidinger, M., E. Buckwar, and H. Hinterleitner (2017). A stochastic version of the Jansen and Rit neural mass model: analysis and numerics. *The Journal of Mathematical Neuroscience* 7(1), 1–35.

Aljalal, M., S. A. Aldosari, M. Molinas, and et al. (2022). Detection of Parkinson’s disease from EEG signals using discrete wavelet transform, different entropy measures, and machine learning techniques. *Sci Rep* 12, 22547.

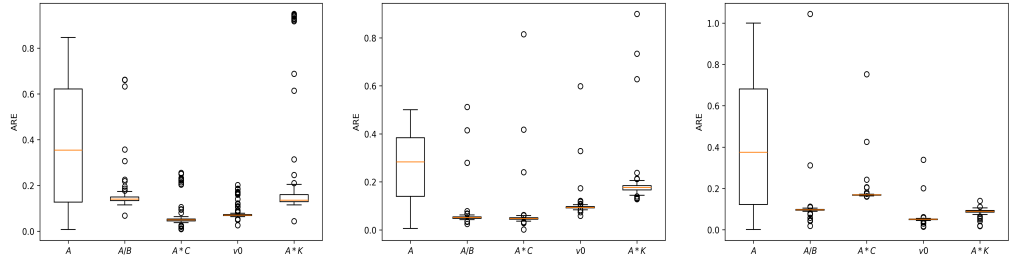


**Figure 14.** Boxplots of ARE values for the estimated parameters  $A_i$ ,  $(A/B)_i$ ,  $(A*C)_i$ ,  $v_{0i}$ , and  $(A*K)_i$  compared to the ground truth values for nodes I–III respectively.

**Table 8.** Median ARE values for parameter estimation in the three-channel system (21)

Parameter	Node I	Node II	Node III
$A$	0.35	0.28	0.37
$A/B$	0.14	0.05	0.10
$A*C$	0.05	0.05	0.17
$A*K$	0.14	0.18	0.09
$v_0$	0.07	0.09	0.05

Anderson, M. J. (2017). *Permutational Multivariate Analysis of Variance (PERMANOVA)*, Chapter 1, pp. 1–15. John Wiley and Sons Ltd.

Arnold, L. (1974). *Stochastic Differential Equations*, Chapter 1-2, pp. 20. Wiley–Blackwell.

Benjamini, Y. and Y. Hochberg (1995). Controlling the false discovery rate: a practical and powerful approach to multiple testing. *Journal of the Royal Statistical Society Series B* 57, 289–300.

Bröhl, T., T. Rings, J. Pukropski, R. von Wrede, and K. Lehnertz (2024). The time-evolving epileptic brain network: concepts, definitions, accomplishments, perspectives. *Frontiers in Network Physiology* 3, 1338864.

Burman, R. J. and R. R. Parrish (2018). The widespread network effects of focal epilepsy. *J. Neurosci.* 38, 8107–8109.

Chen, C., R. N. Henson, K. E. Stephan, J. M. Kilner, and K. J. Friston (2009). Forward and backward connections in the brain: a DCM study of functional asymmetries. *NeuroImage* 45, 453–462.

Chen, K.-T. (1954). Iterated integrals and exponential homomorphisms. *Proc. Lond. Math. Soc.* 4, 502–512.

Choi, G. Y., W. K. Chang, M. Shim, N. Kim, J. H. Jang, W. S. Kim, H. J. Hwang, and N. J. Paik (2023). Electroencephalography network indices as biomarkers of upper limb impairment in chronic stroke. *JoVE* 197, 10.3791/64753.

Courtial, J., M. Guye, F. Bartolomei, S. Petkoski, and V. K. Jirsa (2020). Dynamical mechanisms of interictal resting-state functional connectivity in epilepsy. *J. Neurosci.* 40, 5572–5588.

Ditlevsen, S., M. Tamborrino, and I. Tubikanec (2025). Network inference via approximate bayesian computation: Illustration on a stochastic multipopulation neural mass model. *The Annals of Applied Statistics* 19(4), 3304 – 3329.

---

Duffy, F. H. and H. Als (2012). A stable pattern of EEG spectral coherence distinguishes children with autism from neuro-typical controls - a large case control study. *BMC Medicine* 10, 64.

Fisher, R. S. and et al. (2005). Epileptic seizures and epilepsy: definitions proposed by the International League Against Epilepsy (ILAE) and the International Bureau for Epilepsy (IBE). *Epilepsia* 46, 470–472.

Fliess, M. (1981). Fonctionnelles causales non linéaires et indéterminées non commutatives. *Bull. Soc. Math. France* 109, 3–40.

Forrester, M., J. J. Crofts, S. Sotiropoulos, S. Coombes, and R. O'Dea (2020). The role of node dynamics in shaping emergent functional connectivity patterns in the brain. *Netw Neurosci*. 4, 467–483.

Forrester, M., S. Petros, O. Cattell, Y. Lai, R. D. O'Dea, S. Sotiropoulos, and et al. (2024). Whole brain functional connectivity: Insights from next generation neural mass modelling incorporating electrical synapses. *PLoS Comput Biol* 20, e1012647.

Friston, K., H. Brown, J. Siemerkus, and K. Stephan (2016). The dysconnection hypothesis. *Schizophrenia Research* 176(2-3), 83–94.

Friston, K. J., L. Harrison, and W. Penny (2003). Dynamic causal modelling. *NeuroImage* 19, 1273–1302.

Friston, K. J., K. H. Preller, C. Mathys, H. Cagnan, J. Heinze, A. Razi, and P. Zeidman (2019). Dynamic causal modelling revisited. *NeuroImage* 199, 730–744.

Ghassemkhani, K., K. S. Saroka, and B. T. Dotta (2025). Evaluating EEG complexity and spectral signatures in Alzheimer's disease and frontotemporal dementia: evidence for rostrocaudal asymmetry. *npj Aging* 11, 50.

Grefkes, C., D. A. Nowak, S. B. Eickhoff, M. Dafotakis, J. Küst, H. Karbe, and G. R. Fink (2008). Cortical connectivity after subcortical stroke assessed with functional magnetic resonance imaging. *Annals of Neurology* 63, 236–246.

Grefkes, C., D. A. Nowak, L. E. Wang, M. Dafotakis, S. B. Eickhoff, and G. R. Fink (2010). Modulating cortical connectivity in stroke patients by rTMS assessed with fMRI and dynamic causal modeling. *NeuroImage* 50, 233–242.

Grimbert, F. and O. Faugeras (2006). Bifurcation analysis of jansen's neural mass model. *Neural Computation* 18, 3052–3068.

Hauke, D. J., J. Rodriguez-Sanchez, H. Oloye, L. C. S. Berndt, D. Pinotsis, K. J. Friston, D. H. Mathalon, and R. A. Adams (2025). A canonical microcircuit for estimating excitation/inhibition (E/I) balance. *bioRxiv*.

Herz, D. M., S. B. Eickhoff, A. Løkkegaard, and H. Siebner (2014). Functional neuroimaging of motor control in Parkinson's disease: a meta-analysis. *Human Brain Mapping* 35, 3227–3237.

Honey, C. J., R. Kötter, M. Breakspear, and O. Sporns (2007). Network structure of cerebral cortex shapes functional connectivity on multiple time scales. *Proceedings of the National Academy of Sciences of the United States of America* 104(24), 10240–10245.

Jansen, B. H. and V. Rit (1995). Electroencephalogram and visual evoked potential generation in a mathematical model of coupled cortical columns. *Biological Cybernetics* 73(4), 357–366.

---

Jiang, S., H. Li, L. Liu, D. Yao, and C. Luo (2022). Voxel-wise functional connectivity of the default mode network in epilepsies: A systematic review and meta-analysis. *Curr Neuropharmacol.* 20(1), 254–266.

Kiebel, S. J., J. Daunizeau, and K. J. Friston (2008). A hierarchy of time-scales and the brain. *PLoS Computational Biology* 4, e1000209.

Kulik, S. D., L. Douw, E. van Dellen, M. Steenwijk, J. Guerts, C. Stam, A. Hillebrand, M. Schoonheim, and P. Tewarie (2023). Comparing individual and group-level simulated neurophysiological brain connectivity using the Jansen and Rit neural mass model. *Network Neuroscience* 7, 950–965.

Lee, A. J. (1990). *U-Statistics*, Chapter 1-2, pp. 320. CRC Press.

Leimkuhler, B., C. Matthews, and G. Stoltz (2016). The computation of averages from equilibrium and nonequilibrium Langevin molecular dynamics. *IMA Journal of Numerical Analysis* 36, 13–79.

Li, G., Y. Liu, Y. Zheng, D. Li, X. Liang, Y. Chen, Y. Cui, P. Yap, S. Qiu, H. Zhang, and D. Shen (2020). Large-scale dynamic causal modeling of major depressive disorder based on resting-state functional magnetic resonance imaging. *Human Brain Mapping* 41(4), 865–881.

Li, J., G. Green, S. J. Carr, P. Liu, and J. Zhang (2025). Bayesian inference general procedures for a single-subject test study. *Neuroscience Informatics* 5(2), 100195.

Lyons, T. J. (1998). Differential equations driven by rough signals. *Revista Matemática Iberoamericana* 14(2), 215–310.

Menon, V. (2023). 20 years of the default mode network: A review and synthesis. *Neuron* 111(16), 2469–2487.

Milstein, G. N. and M. V. Tretyakov (2003). Quasi-symplectic methods for Langevin-type equations. *IMA Journal of Numerical Analysis* 23, 593–626.

Ogrim, G., J. Kropotov, and K. Hestad (2012). The quantitative EEG theta/beta ratio in attention deficit/hyperactivity disorder and normal controls: sensitivity, specificity, and behavioral correlates. *Psychiatry Research* 198, 482–488.

OK, F., R. R, and R. K. Ravindren (2021). Scalp EEG recordings of pediatric epilepsy patients: A dataset for automatic detection of interictal epileptiform discharges from routine EEG. *Data in Brief* 39, 107680.

Papadopoulou, M., M. Leite, P. van Mierlo, K. Vonck, L. Lemieux, K. Friston, and D. Marinazzo (2015). Tracking slow modulations in synaptic gain using dynamic causal modelling: Validation in epilepsy. *NeuroImage* 107, 117–126.

Park, B., S. Hong, S. Valk, and et al. (2021). Differences in subcortico-cortical interactions identified from connectome and microcircuit models in autism. *Nat Commun* 12, 2225.

Pereira, I., S. Frässle, J. Heinze, D. Schöbi, C. T. Do, M. Gruber, and K. E. Stephan (2021). Conductance-based dynamic causal modeling: A mathematical review of its application to cross-power spectral densities. *NeuroImage* 245, 118662.

Pokern, Y., A. M. Stuart, and P. Wiberg (2009). Parameter estimation for partially observed hypoelliptic diffusions. *Journal of the Royal Statistical Society Series B: Statistical Methodology* 71(1), 49–73.

---

Pyrzowski, J., M. Siemiński, A. Sarnowska, J. Jedrzejczak, and W. M. Nyka (2015). Interval analysis of interictal EEG: pathology of the alpha rhythm in focal epilepsy. *Scientific Reports* 5, 16230.

Rehme, A. K., G. R. Fink, D. Y. von Cramon, and C. Grefkes (2011). The role of the contralateral motor cortex for motor recovery in the early days after stroke assessed with longitudinal fMRI. *Cereb Cortex* 21, 756–768.

Rosch, R. E., P. R. Hunter, T. Baldeweg, K. J. Friston, and M. P. Meyer (2018). Calcium imaging and dynamic causal modelling reveal brain-wide changes in effective connectivity and synaptic dynamics during epileptic seizures. *PLoS Comput Biol* 14, e1006375.

Singh, M., T. Braver, M. Cole, and S. Ching (2025). Precision data-driven modeling of cortical dynamics reveals person-specific mechanisms underpinning brain electrophysiology. *Proc Natl Acad Sci U S A.* 122, e2409577121.

Sotero, R. C., N. J. Trujillo-Barreto, Y. Iturria-Medina, F. Carbonell, and J. C. Jimenez (2007). Realistically coupled neural mass models can generate EEG rhythms. *Neural Computation* 19, 478–512.

van Es, M. W. J., C. Higgins, C. Gohil, A. J. Quinn, D. Vidaurre, and M. W. Woolrich (2025). Large-scale cortical functional networks are organized in structured cycles. *Nat Neurosci.* 28, 2118–2128.

Wendling, F., E. Koksal-Ersoz, M. Al-Harrach, M. Yochum, I. Merlet, G. Ruffini, F. Bartolomei, and P. Benquet (2024). Multiscale neuro-inspired models for interpretation of EEG signals in patients with epilepsy. *Clinical Neurophysiology* 161, 198–210.

Yang, S., Y. Zhou, C. Peng, and et al. (2024). Macroscale intrinsic dynamics are associated with microcircuit function in focal and generalized epilepsies. *Commun Biol* 7, 145.

Zhang, J. and G. Green (2025). Detecting mild traumatic brain injury with MEG scan data: One-vs-K-sample tests. *Imaging Neuroscience* 3, IMAG.a.137.

Zhang, J. and A. Sanderson (2009). JADE: Adaptive Differential Evolution with Optional External Archive. *IEEE Transactions on Evolutionary Computation* 13, 945–958.

Özbek, Y., E. Fide, and G. G. Yener (2015). Resting-state EEG alpha/theta power ratio discriminates early-onset Alzheimer's disease from healthy controls. *Clinical Neurophysiology : official journal of the international federation of clinical neurophysiology*. *Clinical Neurophysiology : Official Journal of the International Federation of Clinical Neurophysiology* 132, 2019–2031.